








AstroSat Study of the Globular Cluster NGC 2298: Probable Evolutionary Scenarios of Hot Horizontal Branch Stars

Sharmila Rani^{1,2} , Gajendra Pandey¹ , Annapurni Subramaniam¹, Chul Chung³ , Snehalata Sahu¹ , and N. Kameswara Rao¹ 

¹ Indian Institute of Astrophysics, Bangalore, 560034, India; sharmila.rani@iiap.res.in

² Pondicherry University, R.V. Nagar, Kalapet, 605014, Puducherry, India

³ Department of Astronomy & Center for Galaxy Evolution Research, Yonsei University, Seoul 03722, Republic of Korea

Received 2021 July 27; revised 2021 October 8; accepted 2021 October 8; published 2021 December 20

Abstract

We present the far-UV (FUV) photometry of images acquired with UVIT on AstroSat to probe the horizontal branch (HB) population of the Galactic globular cluster NGC 2298. UV-optical color–magnitude diagrams (CMDs) are constructed for member stars in combination with Hubble Space Telescope UV Globular Cluster Survey data for the central region and Gaia and ground-based photometric data for the outer region. A blue HB (BHB) sequence with a spread and four hot HB stars are detected in all FUV-optical CMDs and are compared with theoretical updated BaSTI isochrones and synthetic HB models with a range in helium abundance, suggesting that the hot HB stars are helium enhanced when compared to the BHB. The estimated effective temperature, radius, and luminosity of HB stars, using the best spectral energy distribution fits, were compared with various HB models. BHB stars span a temperature range from 7500 to 12,250 K. Three hot HB stars have 35,000–40,000 K, whereas one star has around $\sim 100,000$ K. We suggest the following evolutionary scenarios: two stars are likely to be the progeny of extreme HB (EHB) stars formed through an early hot-flasher scenario, one is likely to be an EHB star with probable helium enrichment, and the hottest HB star, which is about to enter the white dwarf cooling phase, could have evolved from the BHB phase. Nevertheless, these are interesting spectroscopic targets to understand the late stages of evolution.

Unified Astronomy Thesaurus concepts: Globular star clusters (656); Horizontal branch stars (746); Blue straggler stars (168); Hertzsprung Russell diagram (725)

Supporting material: extended figure

1. Introduction

Galactic globular clusters (GGCs) are one of the oldest (age ~ 10 – 13 Gyr) stellar systems known to exist in our galaxy. It has been well established from the last two decades that globular clusters (GCs) host multiple stellar populations instead of simple stellar populations. Complex populations with different chemical compositions are detected in all phases of stellar evolution, such as the Main Sequence (MS; Piotto et al. 2007), Sub-Giant Branch (SGB; Milone et al. 2008; Anderson et al. 2009; Piotto et al. 2012), Red Giant Branch (RGB; Marino et al. 2008; Yong & Grundahl 2008; Lee et al. 2009; Piotto et al. 2015; Milone et al. 2017, 2018), and Asymptotic Giant Branch (AGB; Lagioia et al. 2021). Helium abundance variations among the distinct sequences along the MS, SGB, and RGB have been found from various photometric and spectroscopic studies within a few clusters (D’Antona et al. 2005; Piotto et al. 2005, 2007; Hema et al. 2020). Recently, Dondoglio et al. (2021) identified and characterized, for the first time, multiple stellar populations along the red horizontal branch (RHB) in 14 GCs based on the distribution of RHB stars in UV-optical two-color diagrams. UV observations are an essential tool to detect and analyze the exotic populations residing in GCs that tend not to follow standard stellar evolution, such as blue straggler stars (BSSs), cataclysmic variables, extreme HB (EHB), and blue-hook (Bhk) stars. Identifying these hot populations in

optical images can be extremely difficult mainly because of two reasons: (1) the severe crowding of optical images (especially in the cores of GCs), which are dominated by MS and RGB stars, and (2) most exotic stars are optically faint and present in the core of the GCs. However, all of these are hotter than other cluster members and emit much of their radiation in the UV. Crowding is generally not a problem in the UV images as normal cluster stars (MS and RGB) are cooler than late A-type stars and considerably fainter at wavelengths less than 2000 Å. Thus, a combination of optical and far-UV (FUV) magnitudes is the most powerful tool to analyze the hot stars in GCs (Ferraro et al. 1998; Dieball et al. 2010; Dalessandro et al. 2011, 2013; Subramaniam et al. 2017; Sahu et al. 2019; Rani et al. 2020, 2021; Singh et al. 2020; Prabhu et al. 2021).

HB stars represent the late stages in the evolution of low-mass stars where helium is burning in the core of mass $\sim 0.5 M_{\odot}$ surrounded by a hydrogen-burning shell (Hoyle & Schwarzschild 1955). The HB is of particular interest as the morphology of the HB varies from cluster to cluster. The change in the HB morphology is actually a well-known problem in GCs and known as the second parameter problem. It has been first suggested that metallicity is a principal parameter governing the shape of HBs in GGCs. In general, metal-rich clusters have red HBs whereas metal-poor ones have stars distributed at higher effective temperatures (bluer colors) along the HB. Moreover, there are several clusters sharing the same metal content, but with different HB morphologies, e.g., the GC pairs M3-M13, NGC 288-NGC 362. Even some metal-rich clusters, namely NGC 6388 and NGC 6441, have blue HBs (Rich et al. 1997; Busso et al. 2007; Dalessandro et al. 2008). These exceptions



Original content from this work may be used under the terms of the [Creative Commons Attribution 4.0 licence](https://creativecommons.org/licenses/by/4.0/). Any further distribution of this work must maintain attribution to the author(s) and the title of the work, journal citation and DOI.

have indicated the need for a second and possibly a third parameter to explain the HB distributions in GCs. Parameters other than metallicity playing a role in shaping the HB are suggested to be age, helium abundance, mass loss along the RGB etc., but the answer is not obvious as some of these parameters are not well constrained from theory. For more information, see Gratton et al. (2010) and references therein. Milone et al. (2014) analyzed the HBs of 74 GGCs using Hubble Space Telescope (HST) data in optical filters and concluded that age and metallicity are the main global parameters, while the range of helium abundance within a GC is the main nonglobal parameter defining the HB morphology. Recently, Tailo et al. (2020) studied the HBs of 46 GCs by comparing the HST data set with theoretical stellar evolutionary models and concluded that helium enhancement and mass loss both contribute to the HB morphology.

The hot subpopulations, namely EHB and BHk, located at the blue and hot end of the BHB, follow a vertical sequence in the optical color–magnitude diagrams (CMDs) as their optical colors become degenerate at high temperatures because of the large increase of the bolometric corrections. In general, EHB and BHk stars are defined as HB stars that have effective temperatures (T_{eff}) higher than $\sim 20,000$ and $\sim 32,000$ K, respectively. BHk stars, also known as subluminescent stars, are fainter than canonical EHB stars in optical as well as in FUV CMDs. They form a hook-like structure at the hot end of the EHB in (FUV – NUV, FUV) CMDs and hence are known as blue-hook stars (see FUV CMDs in D’Cruz et al. 2000; Brown et al. 2001, 2010). The hottest EHB and BHk stars have extremely thin envelope masses ($M_{\text{env}} < 0.01M_{\odot}$) due to severe mass loss on the RGB. Therefore, these stars, when helium is exhausted in their core, evolve into the AGB-manqué stars or post-early AGB (peAGB) stars but do not ascend to the AGB (Greggio & Renzini 1990; Dorman et al. 1993). It is extremely difficult to detect them in optical images due to their faintness and location near the crowded core of GCs. Here, UV CMDs play an important role as these stars are bright compared to the cooler stars in UV images and also they follow a particular sequence in UV CMDs separating them from BHB and hot BSSs. It has been well demonstrated from spectroscopy and spatially resolved imaging that EHB stars are the dominant contributors to the UV upturn in the spectra of elliptical galaxies (Dorman et al. 1995; Brown et al. 1997, 2000, 2008; Chung et al. 2011; Bekki 2012). The dominating mechanism for producing these hot objects in GCs is still unclear. Until now, many theories have been proposed to explain the formation of both types of stars in GCs, although the population of these stars mainly depends on the cluster mass and density (Moehler et al. 2004; Rosenberg et al. 2004). Very massive and dense clusters such as NGC 2808 and ω Cen have large samples of EHB and BHk stars. The possible formation scenarios suggested for EHB and BHk stars in clusters are dynamical interactions among binary stars, helium mixing, early hot flasher, late hot flasher, and helium enhancement (Mengel et al. 1976; Sweigart 1997; Brown et al. 2001, 2010; Lei et al. 2015; Heber 2016).

The southern GGC NGC 2298 is located in the constellation Puppis at a distance of 10.6 kpc and has metallicity $[\text{Fe}/\text{H}] = -1.92$ dex (Carretta et al. 2009; Harris 2010; Monty et al. 2018). The adopted reddening value and age for the cluster in this work are (0.2 ± 0.01) mag and (13.2 ± 0.4) Gyr, respectively (Monty et al. 2018). NGC 2298 is also known for hosting multiple stellar populations along the MS and the RGB (Piotto et al. 2015; Milone et al. 2017). This cluster is widely studied in the optical, but UV studies of this cluster are sparse. As this

cluster is metal poor, its HB mainly comprises BHB and a few EHB stars and hence is ideal for studying the UV properties of the very hot HB population. In our quest to understand the formation and evolution of hot HB stars, here we present, for the first time, an FUV photometric study of hot HB stars in NGC 2298. This work aims to identify and shed light on the properties of hot HB stars in this cluster and find their formation mechanisms in comparison with theory.

The structure of this paper is as follows. Section 2 describes the observational data and their reduction. In Section 3, the proper-motion (PM) membership determination using Gaia EDR3 data is presented. Section 4 presents the selection of HB and BSS samples as well as details of the observed UV and optical CMDs. In Section 5, a comparison of observed HB with theoretical models is discussed. In Sections 6 and 7, we describe the properties of HB stars derived from UVIT photometry along with HST, Gaia, and ground-based photometry and their evolutionary status. A detailed discussion of all results is provided in Section 8. Finally, we summarize and conclude our results in Section 9.

2. Data Used and Analysis

2.1. UVIT Data

To investigate the stellar populations along the HB in GGC NGC 2298, we have used images taken with the UVIT instrument on board the AstroSat satellite. The observations of NGC 2298 were carried out on 13 December 2018 in three FUV filters: F148W, F154W, and F169M. UVIT consists of twin 38 cm telescopes, one for the FUV region (130–180 nm) and the other for the NUV (200–300 nm) and visible (VIS) regions (320–550 nm). UVIT is primarily an imaging instrument, simultaneously generating images in the FUV, NUV, and VIS channels over a circular field of diameter $28'$. Full details on the telescope and instruments, including initial calibration results, can be found in Tandon et al. (2017a). The magnitude system adopted for UVIT filters is similar to that used for GALEX filters, and hence the estimated magnitudes will be in the AB magnitude system.

In order to complete the required exposure times in given filters, UVIT takes data over multiple orbits. A customized software package, CCDLAB (Postma & Leahy 2017), was utilized to correct for the geometric distortion, flat-field illumination, and spacecraft drift and to create images for each orbit. Then, the orbit-wise images were coaligned and combined to generate science-ready images in order to improve the signal-to-noise ratio. The photometry was performed on these final science-ready images to derive the magnitudes of the stars detected with UVIT. A detailed log of UVIT observations of NGC 2298 is reported in Table 1. The color image of NGC 2298 in the F148W band is shown in Figure 1. In this figure, the blue color indicates UVIT FUV detections in the F148W filter. Crowding is not a problem here, as we are able to resolve stars well into the core of the cluster in FUV images.

2.2. Photometry

In order to derive the magnitudes of stellar sources, crowded field photometry was carried out on all FUV images using the DAOPHOT package in IRAF/NOAO (Stetson 1987). The following steps are taken to extract point-spread function (PSF) photometry. At first, the stars were located in the images using

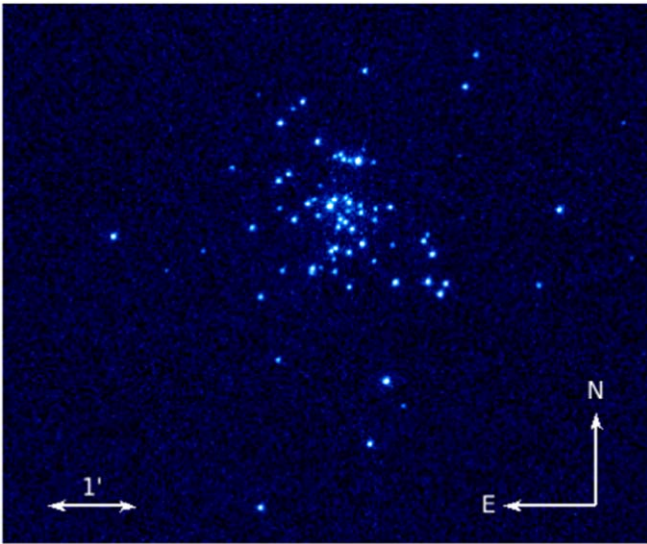


Figure 1. The color image of NGC 2298 in UVIT FUV band F148W. The hot stellar populations displayed in blue are well resolved at the center of the cluster.

Table 1
Observational Details of NGC 2298 in UVIT FUV Filters

Filter	λ_{mean} (Å)	$\Delta\lambda$ (Å)	ZP (AB mag)	Exposure Time (sec)	A_λ (mag)
F148W	1481	500	18.016	2300	1.63
F154W	1541	380	17.78	558	1.59
F169M	1608	290	17.45	1263	1.55

Note. The last column lists the extinction value calculated in each FUV filter using Fitzpatrick’s (1999) law of extinction.

the DAOFIND task, and then the aperture photometric magnitudes were computed using the PHOT task in DAOPHOT. The model PSF was constructed by selecting isolated and bright stars, and then it was applied to all the detected stars using the ALLSTAR task to obtain PSF-fitted magnitudes. A curve-of-growth analysis was carried out to estimate aperture correction values in each filter, which were then applied to the estimated PSF magnitudes. As the detector works in the photon-counting mode, saturation correction (to account for more than one photon per frame), was done to the PSF-generated magnitudes to get the instrumental magnitudes. The saturation correction mainly affects stars brighter than 17 mag. The details of the saturation correction are described in (Tandon et al. 2017b). We have calibrated the instrumental magnitudes into the AB system by using zero-point magnitudes provided in the calibration paper (Tandon et al. 2017b). We show our PSF-fit errors for all filters as a function of magnitude in Figure 2. Stars detected with UVIT are considered up to ~ 22 mag in the FUV F148W filter, and ~ 21 mag in the F154W and F169M filters for further analysis, which effectively puts an upper limit of ~ 0.3 mag on our photometric errors. The observed UVIT stellar magnitudes are corrected for extinction and reddening. To compute the extinction value in the visual band (A_V), we have adopted reddening $E(B - V) = 0.20$ mag from Monty et al. (2018) and the ratio of total-to-selective extinction as $R_V = 3.1$ from Whitford (1958) for the Milky Way. The Fitzpatrick reddening law (Fitzpatrick 1999) was used to calculate extinction coefficients A_λ for all bandpasses as tabulated in Table 1. We adopted the following relation to correct for

extinction and reddening in observed magnitudes:

$$m_{f,\text{corr}} = m_{f,\text{obs}} - c_f R_V E(B - V), \quad (1)$$

where $m_{f,\text{corr}}$ is the extinction corrected magnitude for a particular bandpass f , $m_{f,\text{obs}}$ is the observed PSF magnitude, and $c_f = \frac{A_\lambda}{A_V}$ is the extinction law.

2.3. Other Catalogs

In this study, we have combined UVIT data with UV-optical photometric data from the HST UV legacy survey catalog of GCs in five filters, namely, F275W, F336W, F438W, F606W, and F814W, provided by Nardiello et al. (2018) in the inner region (central region $\sim 2'.7 \times 2'.7$ covered by HST WFC3/UVIS) and for the external region (not observed with HST), we used the optical catalog provided by Stetson et al. (2019) obtained by analyzing ground-based observations. To select the PM members of the cluster in the outer region, the Gaia EDR3 PM catalog is utilized (Gaia Collaboration et al. 2021).

3. Proper-motion Membership

To select the confirmed members of the cluster in the inner region covered by HST, we have used membership probability information given in the astrophotometric catalog of Nardiello et al. (2018). To obtain the membership probability of stars in the outer region of the cluster, we have utilized Gaia EDR3 PM data released on 2020 December 3 (Gaia Collaboration et al. 2021). The Gaia EDR3 catalog provides the photometric and astrometric information for all the stars with Gmag down to 21 mag. We have employed a probabilistic Gaussian mixture model (GMM) method to select member stars in the cluster and infer the intrinsic parameters of the distributions of both member and nonmember stars. The distribution of stellar sources in PM space (μ_α, μ_δ) consists of a well-defined clump corresponding to the cluster members and a wide distribution of field stars. In most clusters, both distributions overlap each other, and we cannot distinguish between the two by eye. Each of the distributions follows a Gaussian distribution, and hence these two distributions are assumed to overlap two Gaussian distributions. The Gaussian probability distribution corresponding to the sum of two distributions is

$$f(\mu|\bar{\mu}_i, \Sigma_i) = \sum_{i=1}^2 w_i \frac{\exp\left[-1/2(\mu - \bar{\mu}_i)^T \Sigma_i^{-1} (\mu - \bar{\mu}_i)\right]}{2\pi \sqrt{\det \Sigma_i}} \quad (2)$$

$$w_i \geq 0, \quad \sum_{i=1}^2 w_i = 1 \quad (3)$$

where μ is the individual PM vector, μ_i are field and cluster mean PMs, Σ is the symmetric covariance matrix, and w_i are weights for the two Gaussian distributions. Full details of this method for an n -dimensional case are described in Vasiliev (2019).

We selected Gaia EDR3 stars with complete astrometric data within twice the tidal radius from the cluster center (de Marchi & Pulone 2007). In order to choose the stars with good astrometric solution, we removed those with parallaxes that deviate by more than 3σ from the expected parallax calculated using the previously known distance to the cluster, where σ is the error in parallax given in Gaia EDR3 catalog. We also removed the sources with renormalized unit weight error

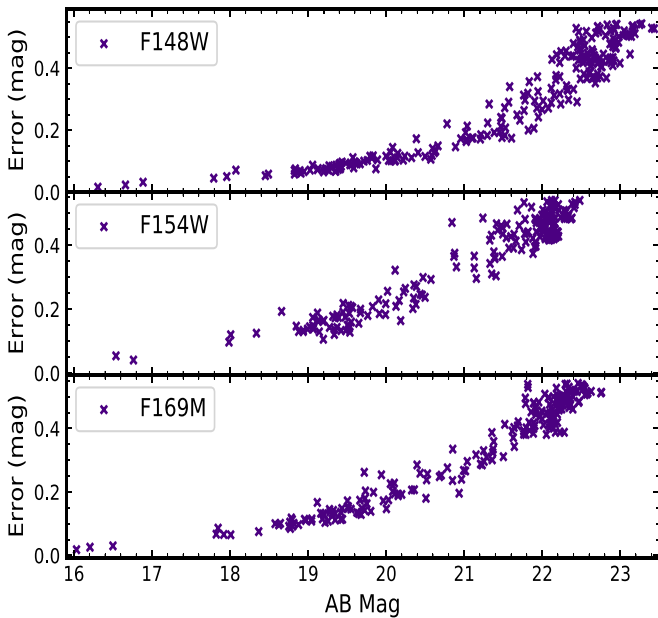


Figure 2. PSF-fit errors as a function of magnitude for our UVIT observations of NGC 2298 in FUV bandpasses. From top to bottom, the panels show results for the F148W, F154W, and F169M bandpasses, respectively.

exceeding 1.2 as larger values of this parameter might lead to an unreliable astrometric solution (Lindegren et al. 2018; Riello et al. 2021). The PMs in R.A. and decl. of the cluster members are supposed to follow two Gaussian distributions. So, GMM is created for these two distributions, and at first, it is assumed that cluster members and field stars follow isotropic Gaussian distributions. Initial guesses for the cluster PM μ_α and μ_δ values and internal velocity dispersion are taken from Vasiliev (2019). We utilized GaiaTools⁴ to maximize the total log-likelihood of GMM and measure the mean PM and standard deviation of both Gaussian distributions. The membership probabilities (MPs) of all the selected stars are calculated using the same technique simultaneously. The equations used to maximize the log-likelihood of GMM and estimate the MP of i th star belonging to the k th component are given in Appendix A in Vasiliev (2019).

We determined the PM mean and standard deviations of the cluster distribution to be $\mu_\alpha = 3.31 \text{ mas yr}^{-1}$ and $\mu_\delta = -2.176 \text{ mas yr}^{-1}$, with $\sigma_c = 0.055 \text{ mas yr}^{-1}$. Figure 3 shows the position of stars in the sky, in the PM space known as vector point diagram (VPD), and in an optical CMD created using Gaia filters. In this figure, blue dots indicate the member stars belonging to the cluster, and gray dots represent the field stars. The stars with an MP of more than 90% are selected as confirmed cluster members. The number of PM members in the outer region of the cluster is found to be ~ 1240 and considered for further analysis.

4. Color–Magnitude Diagrams

4.1. Selection of HB and BS Stars

We have data in three FUV filters of UVIT, and only very hot and bright stars are expected to be detected. It is not easy to classify the stars belonging to different evolutionary sequences from the FUV CMDs. Therefore, optical CMDs are needed to identify different evolutionary sequences. Because UVIT has a

large field of view, it covers the outer parts of the cluster. As GCs are very dense and massive objects, the HST is an ideal telescope to resolve and study the central region of the clusters in all available bandpasses.

In order to identify and classify UVIT-detected stars into various evolutionary phases, we used the HST catalog (Nardiello et al. 2018) to cross-match with our stars inside a central region and ground-based photometric data for the region outside the HST coverage. Nardiello et al. (2018) estimated the PM membership probabilities of stars detected in the inner region of the cluster using HST data and suggested that the most likely members have a PM probability of more than 90%. Therefore, we have selected stars with a membership probability of more than 90% in the inner as well as outer regions using the HST and Gaia EDR3 catalogs, respectively. However, there are four stars in the inner region with a membership probability of more than 80%, which are bright in UV images and found to lie along the HB locus. We have also included these stars in our study. To identify member stars in the outer region of the cluster, we first cross-matched ground-based photometric data (Stetson et al. 2019) with Gaia EDR3 PM membership data. In order to plot stars detected in the inner and outer regions in the same optical ($V - I, I$) CMD, we have transformed the HST ACS/WFC photometric system into the standard Johnson–Cousins photometric system using the transformation equations given in Sirianni et al. (2005). The optical CMD, created using member stars detected with the HST and the ground-based observations, is shown in Figure 4, where filled and open symbols indicate the stars detected in the inner and outer regions, respectively. The magnitude system adopted for the Johnson–Cousins filters is Vega, hence, the $V - I$ color and I magnitude shown in Figure 4 are in the Vega magnitude system.

The HB stars were selected by giving a specific color and magnitude cutoff ($-0.2 < V - I < 1.0$, $14.5 < I < 20.1$) in an optical CMD and indicated with the filled and open red-colored symbols in Figure 4. Because this is a metal-poor cluster, the HB is populated mainly with BHB and hot HB stars. However, there are also one or two RHB stars present along the HB. Because of its low metallicity, very few variable stars such as RR Lyrae were detected in the cluster. Until now, only four RR Lyrae are known in this cluster (Clement et al. 2001). We have cross-matched the HST and ground-based photometric data with the available variable star catalog to identify the cluster’s previously known RR Lyrae stars. The green inverted triangles correspond to the variable stars in Figure 4. In order to select the BSSs in the inner region, we have employed the same approach used by Raso et al. (2017). Their study highlighted the importance of using UV CMDs over optical CMDs for the proper selection of BSSs in GCs. The BSSs are selected from the UV CMD created using the HST F275W and F336W passbands and are shown by the filled blue symbols in Figure 4. BSSs are selected from an optical CMD in the outer region and are displayed with open blue symbols.

4.2. UV and UV-optical CMDs

This section presents the FUV-optical CMDs generated by cross-identifying common stars between optical and our FUV detections. As only hot and bright stars have detectable emission in the FUV, we have cross-matched FUV-detected sources with the above-selected sample of HB and BSSs in the cluster’s inner and outer regions using optical passbands. The

⁴ <https://github.com/GalacticDynamics-Oxford/GaiaTools>

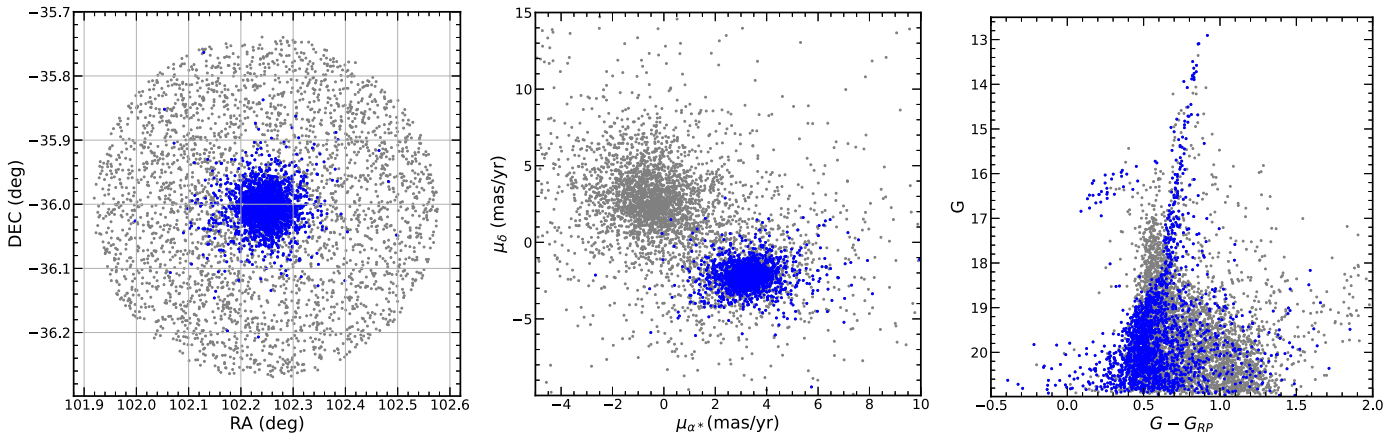


Figure 3. In three panels from left to right, PM members of the cluster are shown with blue dots and the remaining Gaia EDR3 sample marked with gray dots represent field stars. Left panel: position in the sky. Middle panel: vector point diagram (VPD). Right panel: Gaia optical CMD.

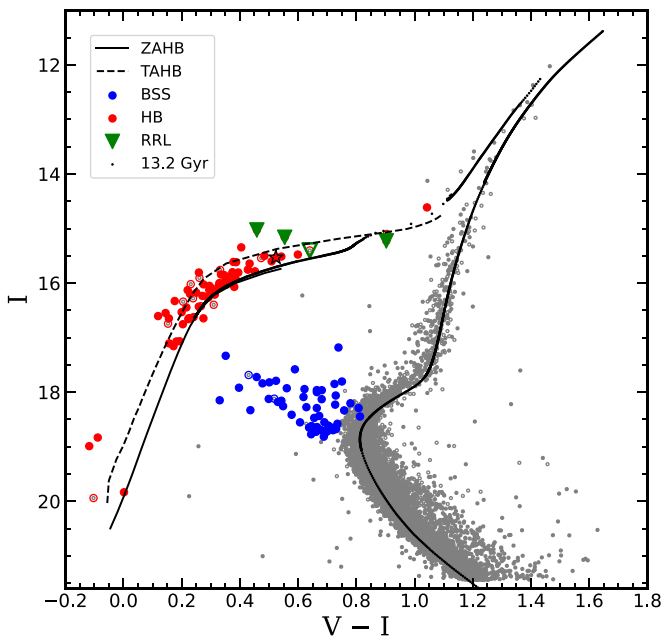


Figure 4. Optical CMD of NGC 2298. Gray dots in the optical CMD represent the HST-detected stars whereas stars shown by gray and colored open symbols are cross-identified using ground-based data and Gaia EDR3 data. All colored symbols represent the selected HB and BS stars used for further cross-matching with UVIT data. All the stars shown in the above CMD are confirmed PM members of the cluster. The known RR Lyrae stars are shown with green inverted triangles. For comparison with theoretical models, we overlaid the updated BaSTI-IAC model isochrone with an age of 13.2 Gyr and metallicity $[\text{Fe}/\text{H}] = -1.92$ dex shown by black dots. Along the HB locus, the solid and dashed black lines indicate zero-age HB (ZAHB) and terminal-age HB (TAHB), where the star has completed 99% of its core He-burning lifetime, respectively.

Vega magnitude system used in the standard Johnson–Cousins photometric system is converted into the AB magnitude system to make it similar to the UVIT magnitude system.

In Figure 5, three panels display the FUV-optical CMDs created using all three FUV filters, where filled and open markers represent the detections in the inner and outer regions, respectively. The photometric error bars shown in all panels of Figure 5 are the median of the photometric errors of stars at a selected magnitude. We have also recovered already known RR Lyrae variables indicated by filled and open green inverted

triangles in all FUV-optical CMDs (See Figure 5). In our FUV images, the variable stars are basically sampled at a random phase. Out of four previously known RR Lyrae stars, we found three in F148W, one in F154W, and two in F169M filter. Their positions in the optical and FUV-optical CMDs are shown in Figures 4 and 5, respectively. We notice that fewer HB stars are detected in the outer region of the cluster when compared to the inner region.

In all CMDs, we detect four stars at the extreme blue end of the HB. These stars are quite separated from the observed HB sequence and are likely to be very hot, as suggested by their FUV-optical color. Out of the four stars, three are found to be brighter and bluer than normal BHB and EHB stars. The three bluer stars might be post-HB (pHB) stars, as evident from their FUV magnitudes in all FUV bands. These hot HB stars are confirmed PM members of the cluster and are well resolved in all FUV images, as shown in Figure 6. The total number of detected BHB, hot HB, BSSs, and variable stars in all UVIT filters are tabulated in Table 2. In the FUV-optical CMDs, we observe that the HB stars no longer lie along the horizontal sequence as found in the optical CMDs; instead, they follow a diagonal sequence with a significant spread. In all FUV CMDs, we also detect a few (up to four) FUV-bright BSSs.

The optical and FUV-optical CMDs overlaid with updated BaSTI-IAC isochrones and HB tracks are shown in Figures 4 and 5, respectively (Hidalgo et al. 2018). The updated BaSTI-IAC⁵ isochrones are considered for an age 13.2 Gyr (Monty et al. 2018), a distance modulus of 15.75 mag (Monty et al. 2018), and a metallicity $[\text{Fe}/\text{H}] = -1.92$ dex (Carretta et al. 2009) with helium abundance $Y_{\text{ini}} = 0.247$, $[\alpha/\text{Fe}] = 0$, encompassing overshooting, diffusion, and mass-loss efficiency parameter $\eta = 0.3$. The BaSTI-IAC model also provides the HB model, which comprises zero-age HB (ZAHB), post-ZAHB tracks, and end of the core-helium-burning phase known as terminal-age HB (TAHB) with or without diffusion for a particular mass range. We have generated the ZAHB and TAHB tracks for a metallicity $[\text{Fe}/\text{H}] = -1.92$ dex, including diffusion happening in the subatmospheric regions of these stars.

The overlaid HB tracks in the FUV CMDs help in defining the location of HB stars, which span an extensive range in color and magnitude, when compared to the optical CMDs. The HB sequence is not well fitted with the theoretical HB models at the

⁵ <http://basti-iac.iaa-brucina.inaf.it/>

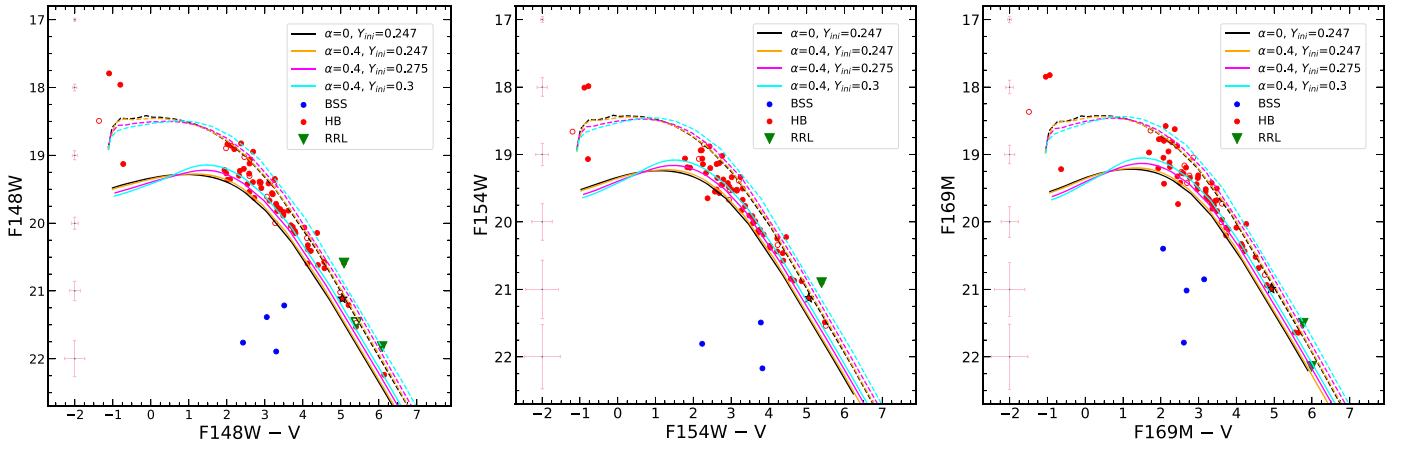


Figure 5. FUV-optical CMDs of NGC 2298. The red filled and open symbols indicate the HB stars detected with UVIT in the inner and outer region of the cluster, respectively. The meaning of different colors and symbols is displayed in the panels. The photometric errors in magnitude and color are also shown in each panel. The solid black line on the HB locus is the ZAHB and the dashed one represents the TAHB for $[\alpha/\text{Fe}] = 0$ and normal helium abundance. The solid and dashed lines, shown in orange, magenta, and cyan color, correspond to alpha-enhanced and helium-enhanced ZAHB and TAHB tracks.

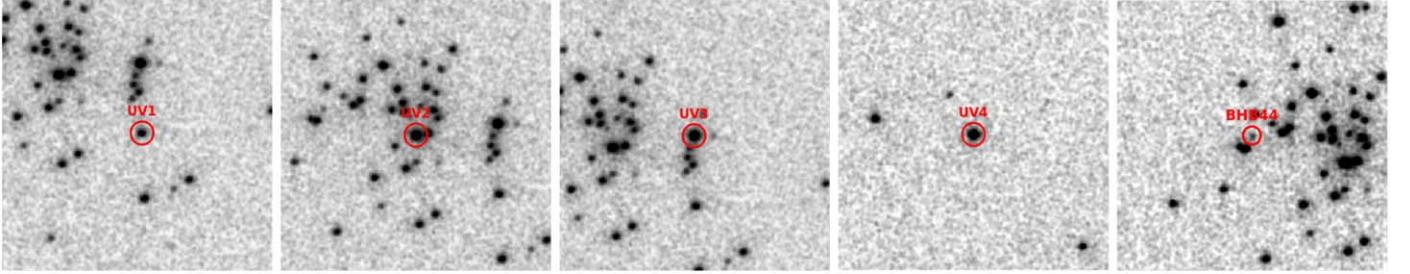


Figure 6. Location of hot HB and BHB44 stars on FUV F148W image of UVIT. The field of view of each image is $2' \times 2'$.

Table 2

The Number of Detected HB and BS Stars in Different UVIT Filters is Listed in this Table

Filter	N_{HB}			N_{BSS}
	N_{BHB}	$N_{\text{Hot-HB}}$	N_{RRL}	
F148W	63(68)	4(4)	3(4)	4
F154W	60(68)	4(4)	1(4)	3
F169M	63(68)	4(4)	2(4)	4

Note. Here N_{HB} and N_{BSS} indicate a number of detected HB and BS stars, respectively. Column 2 displays the subpopulations of HB stars, where N_{BHB} , $N_{\text{Hot-HB}}$, and N_{RRL} denote the number of BHB, hot HB, and RRL identified with UVIT. The total number of selected HB and RRL stars from an optical CMD are shown in parentheses.

brighter end (above 20 mag) with normal helium abundance ($Y_{\text{ini}} = 0.247$ dex) shown by the black solid and dashed lines. The color/magnitude spread at brighter FUV magnitudes might be related to chemical composition differences among BHB stars or the evolutionary effects from ZAHB or photometric errors. In order to probe the cause of this spread, we have compared observations with theoretical HB models generated for enhanced $[\alpha/\text{Fe}] = 0.4$ dex and different initial helium abundances available in the updated BaSTI-IAC database, i.e., $Y_{\text{ini}} = 0.247, 0.275,$ and 0.3 . The ZAHB and TAHB tracks corresponding to these initial helium abundances are indicated

by different color solid and dashed lines in Figure 5, respectively. We find that ZAHB tracks with different initial helium abundances are not producing the color/magnitude spread observed along the BHB sequence in all FUV-optical CMDs. We also notice that HB stars are located between the ZAHB and TAHB tracks, suggesting that some may be evolving from the HB. Out of four hotter HB stars, three stars are found to be brighter than TAHB tracks, indicating that they are in the pHB phase, whereas one is lying within the ZAHB and TAHB tracks, implying that it is an EHB star. In order to confirm the nature of these stars further, effective temperatures and bolometric luminosities are measured using the spectral energy distribution (SED) fitting technique described in Section 6.

5. Comparison with Models

5.1. Synthetic Helium HB Models

We constructed the synthetic HB stellar populations for enhanced $[\alpha/\text{Fe}] = 0.3$ and different initial helium abundances to check for the spread in helium abundance as well as evolution. Chung et al. (2017) demonstrated the implications and prospects for the helium-enhanced populations in relation to the second-generation populations found in the Milky Way GCs using the Yonsei Evolutionary Population Synthesis (YEPS) model. The synthetic HB models presented here are based on Yonsei-Yale (Y^2) stellar evolutionary tracks with

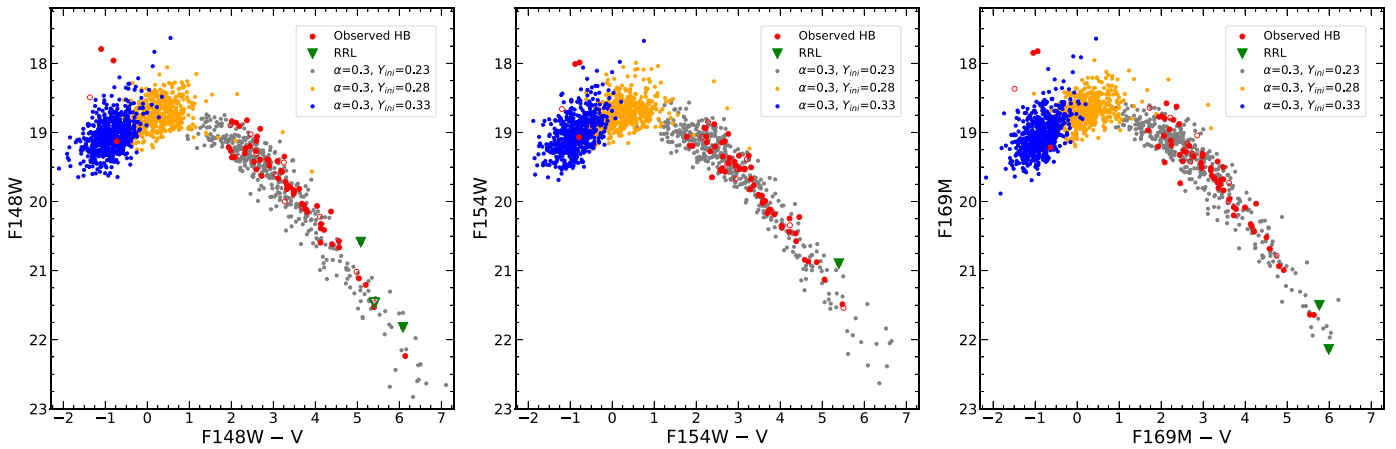


Figure 7. FUV-optical CMDs showing the comparison of the observed HB with synthetic HB models. The meaning of the red and green symbols is the same as in Figure 5. The simulated HB populations for the initial helium abundance $Y_{\text{ini}} = 0.23$, 0.28 , and 0.33 are marked with gray, orange, and blue dots, respectively.

enhanced initial helium abundance (Lee et al. 2015). We choose three values for Y_{ini} as 0.23, 0.28, and 0.33, at a fixed Z value of 0.0002 ($[\text{Fe}/\text{H}] = -1.9$ dex) and age of 13 Gyr (close to the cluster age of 13.2 Gyr). Evolutionary effects from ZAHB and observational photometric errors are taken into account. Figure 7 displays the synthetic CMDs for three different Y_{ini} values, 0.23 (gray), 0.28 (orange), and 0.33 (blue), overlaid on the observed FUV-optical CMD where observed HB stars are highlighted in red. We notice that observations match well with synthetic HB models, especially in the case of BHB stars. It is clear from the comparison of synthetic HB models with observations that all BHB stars have the same helium abundance, implying that BHBs consist of a single $Y_{\text{ini}} = 0.23$. Therefore, we suggest that the color/magnitude spread among BHB stars is not caused by helium variation. Out of four hot HB stars, one star is found to have $Y_{\text{ini}} = 0.33$, and another at the brighter extension appears to be the product of enhanced helium, which, in turn, implies that these stars originated from helium-enhanced populations. The other two hot HB stars are brighter than the simulated stars for $Y_{\text{ini}} = 0.33$, suggesting that they are in an evolved stage and might be the progeny of helium-enhanced EHBs in this cluster. Therefore, using synthetic HB models, we estimate $Y_{\text{ini}} = 0.23$ for BHB stars and four hot BHB stars are likely to have $Y_{\text{ini}} = 0.33$. Thus, enhanced helium abundance seems to play a role in the formation of hot HB stars in this cluster.

5.2. Hot Flasher Models

The location of very hot HB subpopulations known as BHK stars in FUV-optical CMDs is not reproduced by the canonical HB models; this subpopulation is hotter than the hottest point along the ZAHBs (See Figure 8 in Dalessandro et al. 2011). The proposed formation scenarios for very hot HB populations such as EHB and BHK stars in clusters are extreme mass loss on RGB, helium enrichment, helium mixing, and hot flasher. In a hot-flasher scenario, stars experience huge mass loss during the RGB phase, leave the branch before the occurrence of the helium core flash, and move quickly to the He-core white dwarf cooling curve, where they experience a helium flash under conditions of strong electron degeneracy in their core (Castellani & Castellani 1993).

Further, depending upon the location of ignition of helium flash along the white dwarf (WD) cooling sequence, hot-flasher models are classified into two types: early hot flasher and late hot flasher. The details of these scenarios are well described in Brown et al. (2001). The progeny of hot flashers ends up on the hotter and bluer side of normal BHB stars. The stars, which are products of the early hot-flasher scenario, are expected to be hotter and of similar UV magnitudes compared to BHB stars in UV CMDs known as EHB stars, whereas the stars that are hotter and fainter than normal EHB stars in UV CMDs are expected to be late hot flashers. Although we did not detect any BHK star in this cluster, there are three hot HB stars that are brighter than synthetic HB populations, and their location is not reproduced by the ZAHB and TAHB tracks.

In order to check whether the hot HB stars are the product of strong mass loss, we have compared observations with hot-flasher models, i.e., the early hot-flasher and late hot-flasher models. The hot-flasher models were generated in UVIT and Gaia EDR3 filters (Cassisi et al. 2003) (Cassisi 2021, private communication). The hot-flasher models superimposed on the observed hot HB stars are presented in Figure 8. These four stars are marked with the names UV1, UV2, UV3, and UV4 in this study, as shown in Figure 8. Two stars, namely UV2 and UV3, are found to lie close to the early hot-flasher model in all three FUV-optical CMDs, suggesting that they are the progeny of EHB stars formed through an early hot-flasher scenario. We notice that UV2 is slightly brighter than the hot-flasher model. UV4 is lying close to the late hot-flasher model (dashed black line), only in the (F154W, F154W - V) CMD, suggesting that it may be an evolved product of a BHK star. However, in the rest of the FUV-optical CMDs, its location is not reproduced by hot-flasher models. From this comparison, the nature of the UV4 star is not very clear. None of the hot-flasher models reproduce the position of one EHB star designated with UV1, but it is well produced by helium-enhanced synthetic HB models, suggesting that it could be a result of helium enrichment in the cluster. As the stars tend to shift location among the CMDs, locating them in the Hertzsprung–Russell (H-R) diagram will be ideal for evaluating their evolutionary status. Further estimation of atmospheric parameters and comparison with theoretical models in the H-R diagram is required to probe these stars’ evolutionary status in detail and shed more light on their nature.

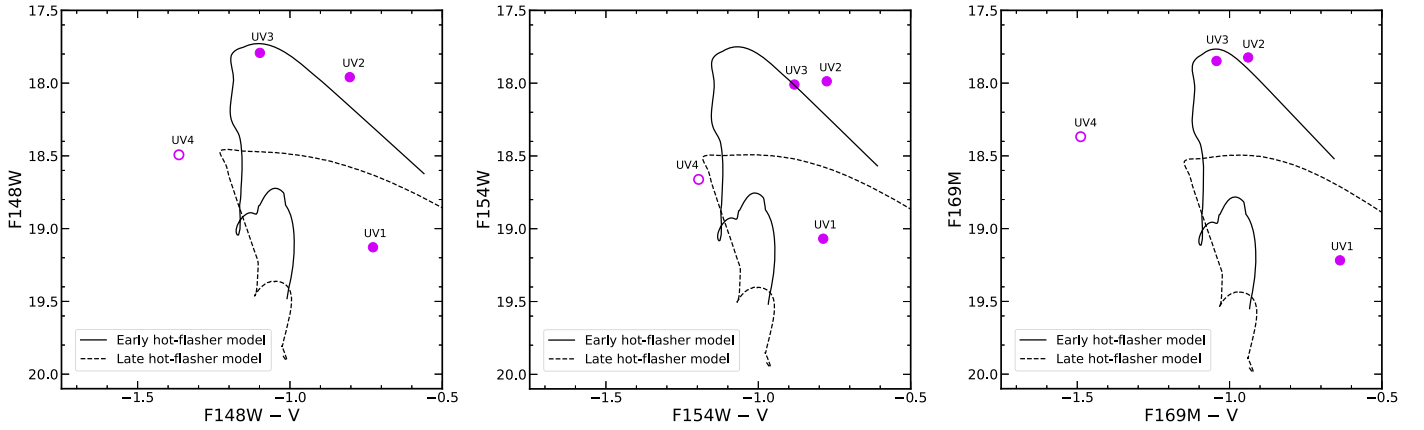


Figure 8. FUV-optical CMDs overplotted with hot-flasher models where the solid and dashed black lines correspond to the early and late hot-flasher models, respectively. The four hot HB stars are indicated by magenta symbols. The filled symbols represent stars within the HST FOV and the open symbol the star in the outer region.

6. Spectral Energy Distribution Fitting

We have detected three hot HB stars in the central region and one in the outer region. As these stars are well separated from the rest of the HB, we aim to check the evolutionary status of these stars by estimating their stellar parameters. In order to estimate the physical parameters like effective temperature (T_{eff}), luminosity ($\frac{L}{L_{\odot}}$), and radius ($\frac{R}{R_{\odot}}$) of the hot HB stars, we constructed their SEDs. SEDs are generated with the observed photometric data points spanning a wavelength range from FUV to IR and fitted with selected theoretical models. We made use of the virtual observatory tool, VOSA (VO SED analyzer; Bayo et al. 2008) for SED analysis. VOSA utilizes the filter transmission curves to calculate the synthetic photometry of the selected theoretical model. By using the fixed distance to the cluster, synthetic fluxes are scaled with the observed fluxes. After constructing the SED, it performs a χ^2 minimization test to compare the observations with the synthetic photometry to derive the best-fit parameters. We computed reduced χ_{red}^2 through the following expression:

$$\chi_{\text{red}}^2 = \frac{1}{N - N_f} \sum_{i=1}^N \frac{(F_{o,i} - M_d F_{m,i})^2}{\sigma_{o,i}^2}, \quad (4)$$

where N is the number of photometric data points, N_f is the number of free parameters in the model, $F_{o,i}$ is the observed flux, $M_d F_{m,i}$ is the model flux of the star, $M_d = \left(\frac{R}{D}\right)^2$ is the scaling factor corresponding to the star (where R is the radius of the star and D is the distance to the star), and $\sigma_{o,i}$ is the error in the observed flux. The number of photometric data points (N) for stars varies from 9 to 13 depending upon their detection in different available filters. The number of free parameters (N_f) used to fit SED are Y_{He} , $\log g$, and effective temperature T_{eff} . The radii of the stars were calculated using scaling factor, M_d .

The Kurucz stellar atmospheric models are employed to construct SEDs (Castelli et al. 1997; Castelli & Kurucz 2003) for HB stars, which have photometry ranging from UV to IR wavelengths. We fixed the value of metallicity $[\text{Fe}/\text{H}] = -2.0$, close to the cluster metallicity, and gave the range of T_{eff} from 5000 to 50,000 K and $\log g$ from 3.5–5 dex in the Kurucz models to fit the SED of HB stars. The locus of ZAHB reflected in the T_{eff} versus $\log g$ plane is used to constrain the range of $\log g$ for HB stars.

We combined three FUV UVIT photometric data points with five HST photometric data points from Nardiello et al. (2018) to create the SED for HB stars detected in the inner region of the cluster. For those detected in the outer region of the cluster, we combined the photometric data points of UVIT (three passbands) with Gaia EDR3 (three passbands) (Gaia Collaboration et al. 2018), ground-based photometry (five passbands) (Stetson et al. 2019), GALEX (two passbands), and 2MASS (three passbands). VOSA makes use of the Fitzpatrick reddening law (Fitzpatrick 1999; Indebetouw et al. 2005) to correct for extinction in observed data points.

It is a well-known fact that HB stars hotter than 11,500 K are affected by atmospheric diffusion, which increases the atmospheric abundances of heavy elements like iron and reduces the atmospheric abundances of light elements. To take this effect into account, we fitted the SEDs of BHB stars with $T_{\text{eff}} > 11,500$ K with solar-metallicity models and determined their atmospheric parameters. As the late hot-flasher scenario predicts enrichment in helium, the non-LTE helium-rich Husfeld models (Husfeld et al. 1989) are used to fit the observed SEDs of four hot HB stars. The model grid covers the range of stellar parameters typical of extremely helium-rich sdO stars: $35,000 \text{ K} \leq T_{\text{eff}} \leq 80,000 \text{ K}$, $4.0 \leq \log g \leq 7.0$, and $0.01 \leq Y_{\text{He}} \leq 0.7$. In the case of the UV4 star, we have noticed that T_{eff} derived using the Kurucz and helium-rich Husfeld model fits to the observed SED corresponds to their upper limit, which indicates that this star is likely to be hotter than the estimated temperature from these models. In order to compute the accurate T_{eff} of this star, we have fitted its SED with the Tübingen NLTE Model Atmosphere Package (TMAP) (Grid4) model used for hot stars (Rauch & Deetjen 2003; Werner et al. 2003). This model grid spans a range of atmospheric parameters such as $20,000 \text{ K} \leq T_{\text{eff}} \leq 150,000 \text{ K}$, $4.0 \leq \log g \leq 9.0$, and $0 \leq X_{\text{H}} \leq 1$. Out of three models used for the SED fit of UV4 star, the TMAP (Grid4) model gives the best fit as indicated from the smaller χ_{red}^2 value tabulated in Table 3.

We carried out SED-fitting analysis for 63 BHB and 4 hot HB stars. Figures 9 and 10 show the SED fit for four hot HB and two BHB stars overplotted with the corresponding best-fit models (smallest value of χ_{red}^2) shown with the light-gray color. In the lower panels of all plots, we show the residuals between the observed SED and the best-fit model. The star ID used in this work, metallicity value of the fitted model

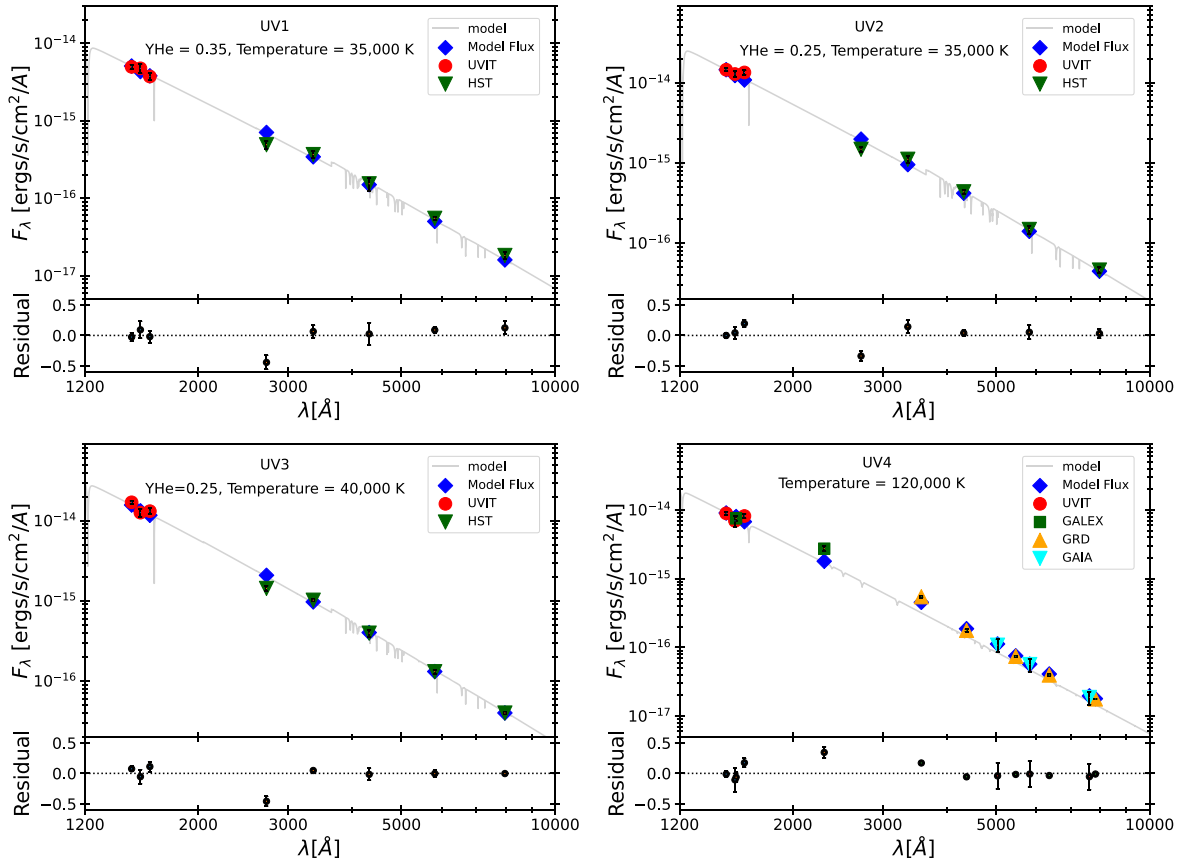


Figure 9. SEDs of four hot HB stars detected with UVIT after correcting for extinction. The stars, denoted UV1, UV2, and UV3, are observed in the inner region of the cluster and UVIT (red) and HST (green) photometric data points are used to create and fit the SED, whereas for UV4, apart from UVIT, GALEX, Gaia EDR3, and ground-based photometric data points are utilized as it is identified in the outer region. Blue diamonds represent the synthetic flux from the helium-rich Husfeld model used to fit the observed SED of UV1, UV2, and UV3 stars, whereas in UV4, they correspond to the TMAP (Grid4) model. The best-fit atmospheric parameters are mentioned in the figure. In UV1, UV2, and UV3 stars, the light-gray solid line represents the theoretical helium-rich Husfeld model spectra and the TMAP (Grid4) model spectra in UV4. The residuals of the SED fit are presented in the bottom panel of all plots.

Table 3
Atmospheric Parameters Derived from SED Fitting of Four Hot HB Stars Detected with UVIT in NGC 2298

Star ID	R.A. (deg)	Decl. (deg)	Model Used	Y_{ini} (dex)	T_{eff} (K)	$\frac{L}{L_{\odot}}$	$\frac{R}{R_{\odot}}$	χ^2_{red}	$\frac{N_{\text{fit}}}{N_{\text{tot}}}$
UV1 ^a	102.2541	−35.99134	Husfeld	0.35	35,000 (35,000–40,000)	36.14 ± 0.12	0.17 ± 0.003	5.1	8/8
			Kurucz		$29,000 \pm 2,000$	27.58 ± 0.12	0.2 ± 0.004	2.8	8/8
UV2 ^a	102.2512	−36.00361	Husfeld	0.25	35,000 (35,000–40,000)	103.9 ± 0.24	0.28 ± 0.005	7.8	8/8
			Kurucz		$32,000^{+4,000}_{-2,000}$	86.39 ± 1.01	0.3 ± 0.006	5.7	8/8
UV3	102.2446	−35.99501	Husfeld	0.25	40,000 (40,000–60,000)	128.3 ± 0.26	0.24 ± 0.004	10.4	8/8
			Kurucz		$50,000_{-7,000}$	235.7 ± 1.06	0.2 ± 0.004	8.7	8/8
UV4 ^a	102.2379	−36.03683	TMAP (Grid4)		120,000 (120,000–150,000)	1148 ± 303.4	0.08 ± 0.002	7.8	13/13
			Husfeld	0.35	80,000 (75,000–80,000)	469.2 ± 17.9	0.11 ± 0.002	10.7	13/13
			Kurucz		$50,000_{-9,000}$	108.5 ± 5.05	0.14 ± 0.003	17.4	11/13

Note. Column 1 lists the star ID used in this work. Columns 2 and 3 display the R.A., decl. of all the stars considered for fitting, respectively. Column 4 presents the different models used for the SED fit of these stars. Columns 5 and 6 list the obtained helium mass fraction and T_{eff} from SED fitting using different theoretical models. The luminosities and radii of these stars along with errors are tabulated in columns 7 and 8, respectively. Columns 9 and 10 list the reduced χ^2 value corresponding to the best fit and ratio of the number of photometric data points ($\frac{N_{\text{fit}}}{N_{\text{tot}}}$) used for the fit to the total number of available data points. Note that stars marked with “a” have estimated temperatures corresponding to the best-fit SEDs and equal to the helium-rich model’s lower or upper limit. The range of temperatures for 10 best fits is also mentioned in the parentheses. The other atmospheric parameters are listed according to the best-fit model.

spectrum, and estimated temperature are displayed in all the SED plots. As mentioned above in Section 4.2, variables such as RR Lyrae are observed at random phases, so we have not considered them for SED analysis. The estimated parameters of

four hot HB stars using the Kurucz, Husfeld, and TMAP (Grid4) models are tabulated in Table 3. The Husfeld model fits find UV1 and UV4 to be much hotter when compared to the estimates from Kurucz model fits, and also suggest these stars

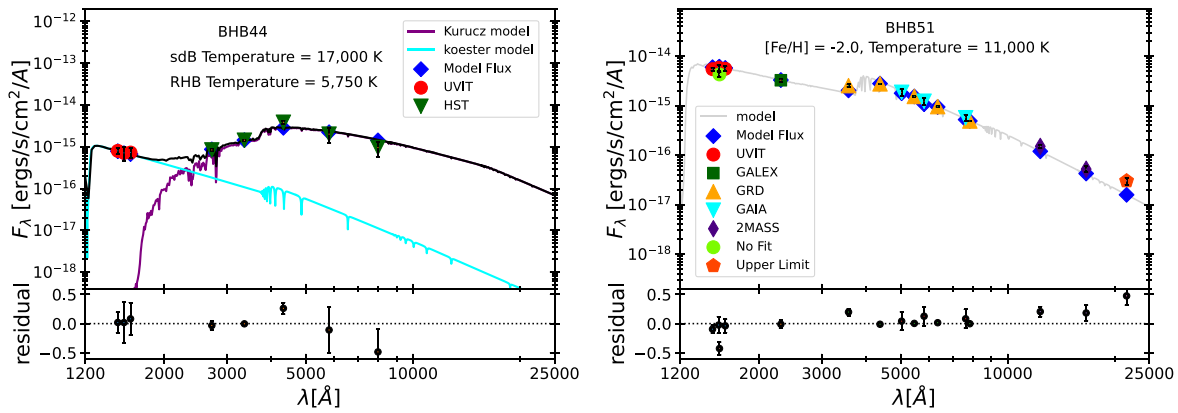


Figure 10. SEDs of BHB stars detected with UVIT in the central (left panel) and outer (right panel) regions after correcting for extinction. The left panel shows the composite SED fit of the BHB44 star where purple and cyan color spectra indicate Kurucz and Koester model spectra as displayed in legend, respectively. The black color represents the composite spectra. The best-fit parameters are displayed in the figure. The rest of the details are the same as in Figure 9.

to be helium rich. On the other hand, the Husfeld model fits to the SEDs of UV2 and UV3 provide normal helium values along with T_{eff} similar to those obtained from the Kurucz model fits (within errors). The T_{eff} (120,000 K) and luminosity ($1148L_{\odot}$) of UV4 obtained using the TMAP (Grid4) model are much higher than estimated from the other two models. The derived values of parameters T_{eff} , $\frac{R}{R_{\odot}}$, and $\frac{L}{L_{\odot}}$ corresponding to the best-fit Kurucz model spectrum along with the errors for BHB stars are listed in Table 4. VOSA computes uncertainties in the effective temperatures as half the grid step, around the best-fit value. As errors estimated through VOSA are not realistic, we have reported the range in T_{eff} as found from the 10 best-fit values. While the $\log g$ values for these stars are also estimated using this technique, these values are not reliable as SED fits are not sensitive to this parameter.

In Figure 9, it can be seen from the residuals that the observed data points are well fitted with the model spectrum. However, in most of the SED fits, the HST F275W data point does not fit with the model flux. The observed flux at F275W is found to be less than the expected flux from the model, which, in turn, gives a negative residual. We note the presence of strong absorption lines such as Fe II and Mg II lines in the wavelength range covered by this filter. It might be possible that there is a mismatch in the strength of these spectral lines between the observations and the models. From the comparison of synthetic Kurucz spectra at different T_{eff} , we notice that the contribution of these lines to the integrated flux of F275W is more at cooler temperatures than the hotter ones, which results in a larger deviation from the expected flux for cooler stars than the hotter stars. In order to establish the best fit to the observed SED, we have only considered the data points that fit well to the model spectra. The high temperatures of UV1 (35,000 K) and UV2 (35,000 K) suggest that they may belong to the class of EHB stars as they have temperatures around 30,000 K (Heber 1986). The other two hot HB stars UV3 and UV4, with very high temperatures of 40,000 and 120,000 K, respectively, might belong to the pHB phase. Also, note that SEDs of all hot HB stars are well fitted with a single spectrum with minimum residual across wavelength, which, in turn, indicates that these are likely to be single stars.

The SEDs of all BHB stars are presented in Appendix. The BHB stars span an effective temperature range from 8000-12,250 K. For one BHB star, namely BHB44, the observed SED is not fitted with a single spectrum as shown in the left panel of Figure 10. Compared to the Kurucz model spectrum and synthetic flux, there

seems to be a large amount of excess flux in FUV filters. We checked whether the star is well resolved in all FUV images (see Figure 6) and also ensured that the cross-identification with the HST catalog is correct. It is located at a distance of 0'.68 from the center of the cluster. It is possible that this star might be a binary star or variable star. If we check the position of this star, marked with a black outlined star symbol in Figures 4 and 5, in optical as well as in UV CMDs, it is lying close to or in the variable region. In the literature, it is not reported as a variable star. The temperature derived from the single fit of BHB44 corresponds to that of an RHB star, which shows significant FUV excess due to a possible hot companion, as RHB stars are too cool to be seen in FUV. In order to check what type of hot companion is present, we fitted the SED with a combination of hot and cool theoretical spectra. To fit the FUV region of the observed SED of this star, we selected a Koester WD model (Koester 2010; Tremblay & Bergeron 2009). The free parameters of the Koester model are T_{eff} and $\log g$. The value for the T_{eff} for the Koester model ranges from 5000 to 80,000 K and $\log g$ from 6.5 to 9.5 dex. We utilized VOSA to obtain the binary fit of this star. The composite SED fit of this star is presented in the left panel of Figure 10 where we can see that the hotter part of SED is well fitted with a Koester model corresponding to a temperature of 17,000 K, and the cooler part is fitted with the Kurucz model of temperature 5750 K. The detailed parameters of both companions are listed in Table 5. The T_{eff} and radius obtained for the cooler part from the best Kurucz model fit correspond to an RHB star. From the T_{eff} and radius, we suggest that the hot companion might belong to the class of subluminous sdB stars (Heber et al. 2003).

Further, to confirm the nature of four hot HB stars, the comparison of the obtained parameters from the SED fit with theoretical evolutionary tracks is needed and discussed in the following section.

7. Evolutionary Status of Hot HB and BHB Stars

The derived atmospheric parameters of hot HB and BHB stars from SED fit are compared with theoretical evolutionary tracks in order to check their evolutionary status. We plotted the theoretical evolutionary tracks employing the models presented by Moehler et al. (2019). The MS to RGB evolutionary track is generated using the updated BaSTI-IAC models presented by Hidalgo et al. (2018). We selected the model with metallicity close to the cluster metallicity. We show the theoretical evolutionary tracks from MS turnoff to the tracks corresponding to different masses starting

Table 4
Atmospheric Parameters Derived from the SED Fit of BHB Stellar Populations Detected with UVIT in NGC 2298

Star ID	R.A. (deg)	Decl. (deg)	T_{eff} (K)	$\frac{L}{L_{\odot}}$	$\frac{R}{R_{\odot}}$	χ^2_{red}	$\frac{N_{\text{fit}}}{N_{\text{tot}}}$
BHB1	102.2435	-36.01081	10,750 ± 250	70.15 ± 1.25	2.38 ± 0.04	3.8	7/8
BHB2	102.2357	-36.01813	12,500 ± 500	43.64 ± 0.59	1.3 ± 0.03	12.7	8/8
BHB3	102.2252	-36.02032	11,500 ± 250	50.83 ± 0.39	1.78 ± 0.03	14.3	8/8
BHB4	102.2281	-36.01802	12,250 ± 500	48.67 ± 1.08	1.5 ± 0.03	4.7	8/8
BHB5	102.2501	-36.00238	10,250 ± 250	73.27 ± 2.46	2.78 ± 0.05	9.2	8/8
BHB6	102.2629	-35.98792	10,500 ± 250	57.85 ± 2.0	2.3 ± 0.04	4.9	8/8
BHB7	102.2271	-36.01273	10,500 ± 250	54.65 ± 1.92	2.23 ± 0.04	8.4	8/8
BHB8	102.2475	-36.00676	10,250 ± 250	44.37 ± 1.59	2.04 ± 0.04	14.1	8/8
BHB9	102.2552	-36.01549	12,000 ± 500	30.79 ± 0.39	1.2 ± 0.02	11.4	8/8
BHB10	102.2459	-36.00806	11,000 ± 250	42.73 ± 1.51	1.79 ± 0.03	6.1	8/8
BHB11	102.2508	-36.0122	12,250 ± 500	33.13 ± 0.47	1.23 ± 0.02	8.9	8/8
BHB12	102.2564	-36.00318	9750 ⁺²⁵⁰ ₋₅₀₀	43.34 ± 1.95	2.26 ± 0.04	35.1	8/8
BHB13	102.2595	-36.0062	11,000 ± 250	39.01 ± 1.63	1.69 ± 0.03	7.4	8/8
BHB14	102.2239	-36.01842	10,250 ± 500	56.95 ± 4.86	2.14 ± 0.04	7.6	8/8
BHB15	102.2633	-35.99884	12,000 ⁺²⁵⁰ ₋₅₀₀	32.35 ± 0.51	1.31 ± 0.03	3.6	8/8
BHB16	102.2467	-36.00291	12,500 ⁺²⁵⁰ ₋₅₀₀	33.43 ± 0.37	1.23 ± 0.02	7.1	8/8
BHB17	102.2439	-36.00493	9750 ⁺⁵⁰⁰ ₋₂₅₀	48.07 ± 1.44	2.42 ± 0.05	13.2	8/8
BHB18	102.2486	-36.00619	10,250 ⁺⁵⁰⁰ ₋₂₅₀	42.13 ± 2.43	1.99 ± 0.04	5.4	8/8
BHB19	102.2498	-36.01167	9250 ⁺⁵⁰⁰ ₋₂₅₀	45.49 ± 1.46	2.53 ± 0.05	16.7	8/8
BHB20	102.2576	-35.98383	9500 ⁺⁵⁰⁰ ₋₂₅₀	53.68 ± 2.26	2.64 ± 0.05	12.1	8/8
BHB21	102.2608	-35.99758	10,500 ⁺⁵⁰⁰ ₋₂₅₀	37.39 ± 1.78	1.79 ± 0.03	6.7	8/8
BHB22	102.2467	-36.01245	10,000 ⁺⁵⁰⁰ ₋₂₅₀	46.03 ± 1.82	2.23 ± 0.04	3.2	8/8
BHB23	102.2292	-36.01033	9500 ± 250	51.97 ± 2.09	2.66 ± 0.05	5.5	8/8
BHB24	102.237	-36.00386	9250 ± 500	49.44 ± 2.62	2.68 ± 0.05	10.8	8/8
BHB25	102.2694	-36.00772	10, 250 ⁺⁵⁰⁰ ₋₂₅₀	33.76 ± 1.81	1.72 ± 0.03	6.9	8/8
BHB26	102.2431	-35.97799	9500 ⁺⁵⁰⁰ ₋₂₅₀	46.76 ± 3.05	2.49 ± 0.05	1.5	8/8
BHB27	102.2673	-36.02095	9750 ⁺⁵⁰⁰ ₋₂₅₀	42.58 ± 3.83	2.09 ± 0.04	2.7	8/8
BHB28	102.2465	-36.01901	9000 ± 500	54.19 ± 2.11	2.95 ± 0.06	8.0	8/8
BHB29	102.248	-35.99478	9500 ⁺²⁵⁰ ₋₅₀₀	44.69 ± 2.14	2.41 ± 0.05	5.2	8/8
BHB30	102.2554	-36.01623	9250 ⁺²⁵⁰ ₋₂₅₀	41.46 ± 3.01	2.24 ± 0.04	7.9	8/8
BHB31	102.2475	-36.00208	9250 ⁺⁵⁰⁰ ₋₂₅₀	45.92 ± 2.18	2.52 ± 0.05	8.6	8/8
BHB32	102.2441	-36.00356	9250 ⁺¹⁰⁰⁰ ₋₂₅₀	38.76 ± 2.55	2.08 ± 0.04	12.5	8/8
BHB33	102.25	-36.01609	9000 ⁺⁵⁰⁰ ₋₂₅₀	46.43 ± 3.92	2.75 ± 0.05	2.7	8/8
BHB34	102.2466	-35.99503	9000 ⁺⁷⁵⁰ ₋₂₅₀	41.83 ± 3.11	2.36 ± 0.04	6.1	8/8
BHB35	102.2407	-36.00629	9750 ⁺⁵⁰⁰ ₋₇₅₀	58.94 ± 4.15	3.19 ± 0.06	9.5	8/8
BHB36	102.2623	-36.01596	9000 ± 500	43.43 ± 2.52	2.53 ± 0.05	7.5	8/8
BHB37	102.2406	-36.0042	8750 ⁺⁵⁰⁰ ₋₂₅₀	48.16 ± 2.15	2.97 ± 0.06	12.2	8/8
BHB38	102.2408	-36.01402	8500 ⁺⁵⁰⁰ ₋₁₀₀₀	77.59 ± 3.12	4.03 ± 0.08	1.8	7/8
BHB39	102.2499	-35.99423	8750 ⁺⁵⁰⁰ ₋₇₅₀	44.66 ± 2.54	2.81 ± 0.05	11.7	8/8
BHB40	102.2469	-36.00461	8500 ± 500	46.42 ± 6.17	2.97 ± 0.06	9.9	8/8
BHB41	102.2284	-36.00907	8500 ± 500	52.18 ± 6.35	3.01 ± 0.06	5.1	8/8
BHB42	102.2741	-35.99637	8750 ⁺²⁵⁰ ₋₅₀₀	40.41 ± 2.48	2.73 ± 0.05	2.0	8/8
BHB43	102.2631	-36.00405	8250 ⁺⁵⁰⁰ ₋₇₅₀	48.52 ± 3.31	3.34 ± 0.06	10.6	8/8
BHB45	102.2548	-36.00226	8500 ⁺⁵⁰⁰ ₋₁₀₀₀	49.53 ± 3.74	3.15 ± 0.06	12.4	8/8
BHB46	102.241	-35.99525	8250 ⁺⁵⁰⁰ ₋₇₅₀	54.8 ± 3.61	3.52 ± 0.07	5.3	8/8
BHB47	102.2486	-35.99375	9500 ⁺⁵⁰⁰ ₋₂₅₀	41.89 ± 2.25	2.27 ± 0.04	8.6	8/8
BHB48	102.2521	-36.01067	7750 ± 500	51.41 ± 2.84	3.8 ± 0.07	14.0	6/6
BHB49	102.2503	-36.01369	8000 ± 125	51.16 ± 4.78	3.65 ± 0.07	32.9	8/8
BHB50	102.1974	-36.0043	12,250 ± 250	53.02 ± 2.62	1.59 ± 0.03	1.2	15/16
BHB51	102.302	-36.00933	11, 000 ⁺²⁵⁰ ₋₅₀₀	62.62 ± 3.29	2.15 ± 0.04	2.0	15/16
BHB52	102.2673	-36.06088	10, 000 ⁺²⁵⁰ ₋₅₀₀	46.22 ± 6.76	2.22 ± 0.04	3.9	15/16
BHB53	102.2418	-36.04874	10, 250 ⁺²⁵⁰ ₋₅₀₀	54.08 ± 8.19	2.32 ± 0.04	3.9	15/16
BHB54	102.1568	-36.10535	9500 ± 250	66.63 ± 4.47	2.99 ± 0.06	0.74	15/16
BHB55	102.2196	-35.98094	10,000 ± 500	52.23 ± 6.51	2.39 ± 0.05	2.6	15/16
BHB56	102.2171	-35.97486	9750 ⁺²⁵⁰ ₋₇₅₀	43.27 ± 6.56	2.27 ± 0.04	1.4	15/16
BHB57	102.2633	-36.03276	8750 ⁺²⁵⁰ ₋₅₀₀	50.34 ± 10.56	3.01 ± 0.06	1.7	15/16
BHB58	102.2021	-36.01866	8750 ⁺²⁵⁰ ₋₅₀₀	64.73 ± 11.11	3.44 ± 0.06	1.8	15/16
BHB59	102.2339	-36.04152	8000 ⁺²⁵⁰ ₋₅₀₀	65.59 ± 5.47	4.16 ± 0.08	3.5	11/11
BHB60	102.2492	-36.00759	10, 750 ⁺²⁵⁰ ₋₅₀₀	35.41 ± 2.0	1.62 ± 0.03	7.9	8/8

Table 4
(Continued)

Star ID	R.A. (deg)	Decl. (deg)	T_{eff} (K)	$\frac{L}{L_{\odot}}$	$\frac{R}{R_{\odot}}$	χ^2_{red}	$\frac{N_{\text{fit}}}{N_{\text{tot}}}$
BHB61	102.2539	-36.00547	9250^{+500}_{-250}	47.15 ± 2.99	2.61 ± 0.05	3.5	8/8
BHB62	102.2809	-36.01208	8250 ± 500	54.26 ± 4.36	3.36 ± 0.06	2.7	6/6
BHB63	102.2535	-35.99972	8000 ± 500	49.49 ± 3.77	3.48 ± 0.07	3.0	7/7

Note. The notation of all columns is the same as in Table 3.

Table 5
Derived Parameters of the BHB44 Star from the Composite SED Fit

Star ID	R.A. (deg)	Decl. (deg)	Type	Model Used	T_{eff} (K)	$\frac{L}{L_{\odot}}$	$\frac{R}{R_{\odot}}$	χ^2_{red}	$\frac{N_{\text{fit}}}{N_{\text{tot}}}$
BHB44	102.2532	-36.01526	sdB	Koester	$17,000 \pm 1000$	4.46 ± 0.23	0.24 ± 0.005	2.9	8/8
			RHB	Kurucz	5750 ± 125	63.38 ± 5.7	8.17 ± 0.15		

from the ZAHB through to a point late in the pHB evolution or a point on the pAGB cooling sequence in Figure 11. The ZAHB and TAHB, representing the end of the HB phase, are shown with a dashed and dashed-dotted line in Figure 11. We also have plotted the early hot-flasher and late hot-flasher tracks shown with magenta and black solid lines. The parameters estimated from the best SED fit for hot HB and BHB stars are plotted in the H-R diagram and shown with different symbols and colors. We can see in Figure 11 that most of the BHB stars marked with red crosses are lying along the BHB tracks shown with blue lines. Nevertheless, there are a few BHB stars, indicated by purple crosses, lying above the TAHB, indicating that these stars' cores have already run out of helium and they have started evolving toward the pHB or peAGB phase.

To compare the estimated parameters of hot HB stars computed using different models, we plotted the hot HB stars' location in the H-R diagram as shown in Figure 11. As the hot HB star UV1 was found to be helium rich by the synthetic HB models, we have shown only the location of this star in the H-R diagram as found from the helium-rich Husfeld model. UV1 is found to be located between the ZAHB and TAHB and slightly hotter than the EHB track for $0.502 M_{\odot}$. Thus, UV1 is still in the HB evolutionary phase, which implies that it is an EHB star, as also seen from Figures 5 and 7. Figure 11 shows that the hot HB star UV2 is found along the AGB-manqué evolutionary stage, corresponding to the initial EHB mass range $0.506\text{--}0.51 M_{\odot}$, which is likely to evolve from the EHB phase. Stars UV3 and UV4 are found to be much hotter and brighter than the EHB tracks. UV3 is found to be located close to the evolutionary track corresponding to an early hot flasher. We infer from here that UV3 is the progeny of an EHB star (with $\sim 0.502 M_{\odot}$) formed through an early hot-flasher scenario. The position of the UV4 star indicates that it might have crossed the post-early-AGB (p(e)AGB) stage and is about to enter the WD cooling stage. TMAP (Grid4) model parameter estimates for the UV4 star suggest that it is a product of a BHB star with a mass of $\sim 0.7 M_{\odot}$. From the model, the mass of the EHB star UV1, turns out to be $0.502 M_{\odot}$. The rest of the hot stars are likely to be evolved from the EHB stars with a ZAHB mass of $\sim 0.5 M_{\odot}$. In comparison, the BHB stars have masses in the range $0.6\text{--}0.75 M_{\odot}$. This suggests that the hot HB stars have lost $\sim 0.1\text{--}0.2 M_{\odot}$ more envelope mass due to mass loss in the RGB. The reason for this enhanced mass loss could be many, including enhanced helium due to mixing, binary interactions, high rotation, etc. In the case of the BHB44 star, a comparison of the L and T_{eff} of the hot companion with the theoretical evolutionary sequences for

extremely low-mass (ELM) WDs computed by Althaus et al. (2013) suggests that it has a low mass of $\sim 0.187 M_{\odot}$. As the mass of the sdB is too low to support the core-helium burning, it might be evolving into a helium-core WD and is likely to be an ELM WD candidate. Therefore, this binary is most likely to be a post-mass-transfer system, consisting of an ELM WD candidate and an RHB star.

The expected number of pHB stars in the cluster is estimated based on the fact that the number of stars in two post-MS phases, in general, will be proportional to the ratio of the lifetimes of these phases (Knigge et al. 2002). The following relation is used to calculate the expected number of pHB stars:

$$N_{\text{pHB}} = N_{\text{HB}} \left(\frac{\tau_{\text{pHB}}}{\tau_{\text{HB}}} \right),$$

where N_{pHB} is the expected number of pHB stars in NGC 2298, N_{HB} is the number of HB stars in the cluster, and τ_{pHB} and τ_{HB} represent the lifetimes of the pHB and HB evolutionary phases of a low-mass star, respectively. We have taken the duration of the HB phase to be $\tau_{\text{HB}} = \sim 10^8$ yr (Dorman 1992) and that of the pHB phase to be $\sim 10^7$ yr from BaSTI pHB tracks. We therefore estimate the number of expected pHB stars to be ~ 7 . The observed number of pHB stars is six in this cluster, which is in fair agreement with the theoretically expected number.

8. Discussion

We have analyzed the UVIT data aboard the AstroSat satellite covering the GC NGC 2298 to characterize the hot HB population in order to understand their formation and evolution. To date, this cluster has been studied in UV, only as part of the group, for comparative studies of HB morphology. A focused study on the HB population of this cluster has not been done so far. This is the first time hot HB stars are characterized in this cluster using FUV photometric data combined with the HST and ground-based data. We combined FUV photometric data with optical photometry to generate the FUV-optical CMDs in three FUV filters (F148W, F154W, F169M) and detected the BHB, four hot HB, and a few bright BS stars.

Brown et al. (2016) analyzed the 53 GGCs using HST UV and blue photometric data to explore the HB morphology, including NGC 2298. They created color-color plots for all selected clusters and found two hot HB stars bluer than the gap between EHB and BHB stars in NGC 2298. They classified these two hot HB stars as

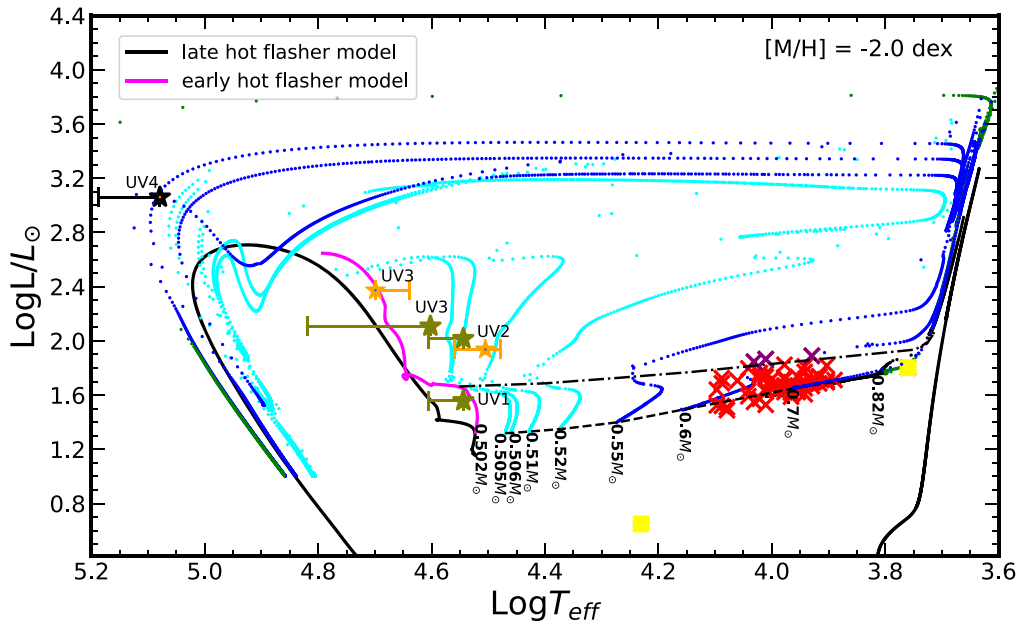


Figure 11. Position of hot HB and BHB stars identified with UVIT in NGC 2298 in the H-R diagram along with theoretical evolutionary tracks. The evolutionary tracks starting from the MS turnoff to the moment when a star has entered the WD cooling phase (Hidalgo et al. 2018) are presented in this plot. Along the HB phase, post-ZAHB tracks span a mass range from 0.502 to $0.82 M_{\odot}$. In the plot, cyan, blue, and green colors correspond to the sequences populating the extreme blue and red parts of the HB. The black dashed and dashed-dotted lines show the position of the canonical ZAHB and TAHB, respectively. The black and magenta solid lines indicate the late and early hot-flasher models, respectively. The SED fit parameters obtained from the Kurucz model fit to the observed SEDs of hot HB and BHB stars are shown with orange star and red cross symbols, respectively. The olive and black filled star symbols present the location of hot HB stars corresponding to the helium-rich Husfeld and TMAP (Grid4) model fits, respectively. Yellow square symbols present the location of the hot and cool companions of the BHB44 star. Several BHB stars evolving toward the peAGB phase are shown with purple cross symbols.

BHk stars based on their location in the color-color plot. In our FUV images, we have detected three hot HB stars in the central region and one in the outer region. In FUV CMDs, out of four hot HB stars, three are brighter than canonical EHB stars and classified as pHB stars.

Schiavon et al. (2012) presented the UV CMDs for 44 GGCs using GALEX photometric data in NUV and FUV passbands, including NGC 2298. They had detected HB and BS stars in NGC 2298, but the sample had issues because of the limited spatial resolution of GALEX and lack of membership analysis for detected stars. Our study detected more than 90% of HB stars compared to the HST and ground-based catalogs, and the PM membership is also confirmed. The stars which are not detected in the FUV images are fainter than the limiting magnitude of UVIT, and the exposure times in all filters are not deep enough to detect them.

Further, we compared the observed HB sequence with theoretical ZAHB and TAHB sequences for standard and enhanced initial helium abundances. The theoretical ZAHB tracks with distinct initial helium abundances could not reproduce the observed color spread along the BHB sequence. Milone et al. (2018) determined the average helium difference between the second-generation and first-generation stars along the RGB in a large sample of 57 GGCs and the maximum helium variation within each GC. The maximum helium variation was found to be 0.011 dex in NGC 2298. Our study does not support a large spread in helium along the BHB sequence, based on a comparison of observed HB with theoretical tracks and synthetic HB, though we detect a possible helium difference of 0.1 dex between the BHB stars and the hot HB stars, as suggested by the synthetic HB simulations.

Wenderoth et al. (1994) presented a spectroscopic study of an extremely blue star in NGC 2298, classifying it as a helium-rich O-type subdwarf star (sdO), but they could not confirm the membership of this star. In their optical CMD shown in

Figure 1, the position of this star coincides with that of EHB or BHk stars. The R.A. and decl. information of this star is not provided in the above paper. Therefore, we could not check whether this star is detected in our FUV images or not.

It is well established from photometric as well as from spectroscopic studies that most of the GCs like NGC 2808 and ω Cen, with well-populated HBs, contain helium-rich populations showing discrete HBs, which indicate discrete helium abundances (Dalessandro et al. 2011; Moehler et al. 2011; Marino et al. 2014). The four hot HB stars in NGC 2298 are found to be helium rich with respect to BHB stars with a standard helium abundance. This may suggest that these stars are products of helium-rich second-generation stars in this cluster. However, the helium-rich population will be hard to be detected due to their small number fraction compared to the normal or slightly enhanced initial helium abundance in the MS to RGB stages of NGC 2298.

Our T_{eff} estimation for three hot HB stars covers a range from 35,000 to 40,000 K, whereas BHB stars span a T_{eff} range from 7500 to 12,250 K. We could not accurately estimate the T_{eff} of the UV4 star, but the temperature of this star can be around $\sim 100,000$ K. A comparison of both T_{eff} and luminosity of hot HB stars with evolutionary tracks implies that three stars have evolved away from the HB and one is still in EHB phase. The hot HB stars also have lost more mass in the RGB (~ 0.1 – $0.2 M_{\odot}$ than the BHB stars).

Many authors put forward several formation scenarios to explain the formation of EHB and BHk stars in GCs other than helium enrichment. Lei et al. (2015) suggested that BHk stars could be the product of binary interactions as tidally enhanced stellar wind in binary evolution might provide the substantial mass loss on the RGB and produce BHk stars. Nevertheless, our SED fits of hot HB stars do not show signature of binarity,

and hence could not support the origin through the binary interaction scenario. The other formation channel suggested for EHB and BHK stars, such as the hot-flasher scenario, is described in detail in Section 5.2. Sweigart (1997) demonstrated that when stars undergo a late helium-core flash on the WD cooling curve, flash mixing of the hydrogen envelope with the helium core will extensively enhance the envelope helium and carbon abundances. In contrast, mixing cannot occur in the early hot-flasher scenario because the large entropy barrier of a strong hydrogen-burning shell prevents the products of core-helium burning from being mixed to the surface.

Brown et al. (2012) presented the HST FUV spectroscopy of hot HB stars including one pHB, five BHB, and three unclassified stars with blue UV colors in GC NGC 2808. They also found enhanced helium and carbon abundances in their BHK sample, which could be the result of flash mixing in the late hot-flasher mechanism, whereas EHB stars in their sample exhibit carbon abundances much lower than the cluster value, and helium abundances at or below the solar value, that could be the effect of diffusion. The two hot HB stars in our study, UV2 and UV3, are found close to early hot-flasher tracks, whereas UV4 is located above the post-BHB track, indicating that UV2 and UV3 could be offspring of EHB stars, and UV4 is a plausible progeny of the BHB star. Therefore, the surface abundances of three stars except UV4 are expected to remain the same if they are products of the early hot-flasher scenario. Nevertheless, these stars could have helium enrichment, as evident from a comparison with simulations. Further spectroscopic follow-up observations are required to confirm the nature of the evolutionary process these stars have gone through.

9. Summary and Conclusions

The main results from this work can be summarized as follows:

1. In this study, we employed UVIT observations in combination with HST, Gaia EDR3, and ground-based photometric data to examine the HB morphology of the GC NGC 2298. Gaia EDR3 data is utilized to obtain the PM members of the cluster in the outer region of the cluster.
2. We constructed optical and FUV-optical CMDs for the member stars. Only the BHB and four hot HB stars are detected in all FUV images. Very few BSSs, which are hot and bright, are detected in FUV CMDs.
3. Optical and FUV-optical CMDs are overlaid with updated BaSTI-IAC isochrones generated for the respective filters to compare the observations with theoretical predictions. The theoretical HB tracks with enhanced alpha and helium abundances could not reproduce the observed color/magnitude spread among BHB stars in FUV-optical CMDs.
4. From the comparison of the observed HB with synthetic HB simulations, we found a helium abundance difference between the BHB and hot HB stars (helium enhanced) in this cluster. However, BHB stars have a single initial helium abundance ($Y_{ini}=0.23$), with probably a very small scatter.
5. We estimated T_{eff} , luminosities, and radii of 63 BHB and 4 hot HB stars by generating SEDs using multiwavelength data. The T_{eff} of BHB stars ranges from 7500 to

12,250 K whereas three hot HB stars span T_{eff} from 35,000 to 40,000 K. The temperature of the UV4 star is found to be around $\sim 100,000$ K.

6. The evolutionary status of HB stars is probed by comparing derived parameters with theoretical evolutionary post-ZAHB tracks. Many BHB stars are found to be located between the ZAHB and TAHB, suggesting that they are evolving off the HB into the pHB phase. These stars have mass in the range of $0.6\text{--}0.75 M_{\odot}$. Some of the BHB stars are found to be evolving toward the pAGB phase.
7. We found a subluminal sdB companion to an RHB star in the cluster. From the comparison with the ELM WD evolutionary tracks, the mass of the sdB turns out to be $\sim 0.187 M_{\odot}$ and likely to be evolving into a helium-core WD. We suggest that it is probably an ELM WD candidate formed from mass transfer in this binary system.
8. Out of four hot HB stars, we find that two already evolved off the EHB phase, and they are in the AGB-manqué phase. One star is located between the ZAHB and TAHB tracks, and hence it is a confirmed EHB star, likely to be helium enriched. One star is found to match with the theoretical prediction of the early hot-flasher scenario (and maybe one more), whereas another star (UV4) has evolved off the p(e)AGB phase and is probably evolving toward the WD cooling stage. The theoretically expected number of pHB stars is found to agree well with the observed number.
9. As the late and early hot flashers are supposed to have different chemical signatures, the pHB stars are targets for further spectroscopic studies in order to explore their nature to constrain their formation pathways.

We thank the anonymous referee for a constructive report that improved the quality of our manuscript. We would like to thank Santi Cassisi for providing us with the hot-flasher models for UVIT filters. C.C. acknowledges the support provided by the National Research Foundation of Korea to the Center for Galaxy Evolution Research (No. 2017R1A2B3002919). S.R. thanks Deepthi S. Prabhu for useful discussions. This publication utilizes the data from AstroSat mission's UVIT, which is archived at the Indian Space Science Data Centre. The UVIT project is a result of collaboration between IIA, Bengaluru, IUCAA, Pune, TIFR, Mumbai, several centers of ISRO, and CSA. This research made use of VOSA, developed under the Spanish Virtual Observatory project supported by the Spanish MINECO through grant AyA2017-84089. This research also made use of Aladin sky atlas developed at CDS, Strasbourg Observatory, France (Bonnarel et al. 2000).

Software: GaiaTools (Vasiliev 2019), Topcat (Taylor 2011), Matplotlib (Hunter 2007), NumPy (van der Walt et al. 2011), Scipy (Oliphant 2007; Millman & Aivazis 2011), Astropy (Astropy Collaboration et al. 2013, 2018) and Pandas (McKinney 2010).

Appendix SED Fitting for BHB Stars

The details of the SED-fitting technique are described in Section 6. The SEDs for 61 BHB stars are shown in Figure 12.

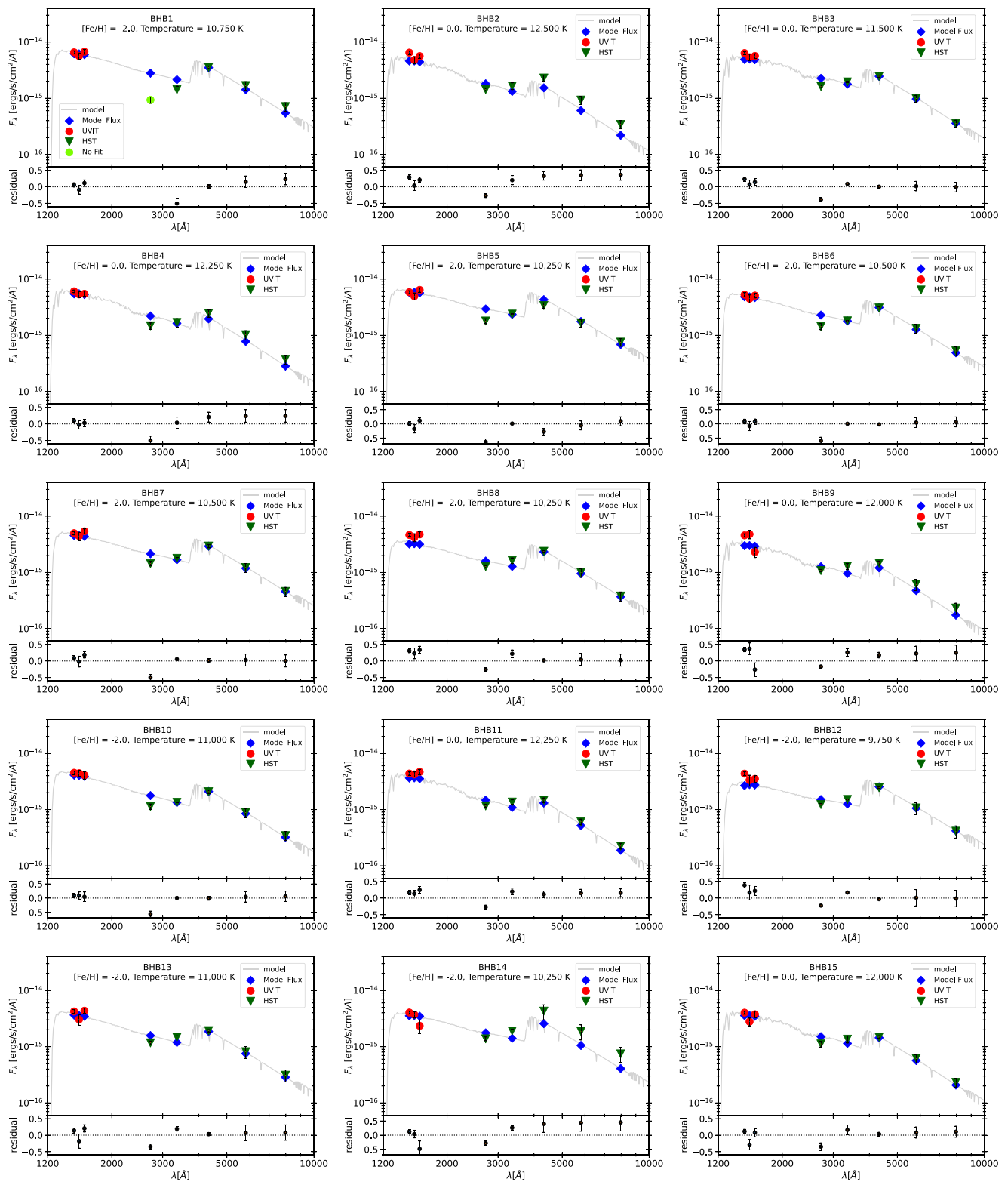


Figure 12. SEDs of the rest of the BHB stars. The best-fit parameters are mentioned in the figure. The UVIT and HST data points used to create SEDs for stars lying in the inner region are shown with red circles and green inverted triangles, respectively. For the stars lying in the outer region, UVIT, GALEX, ground-based photometric, Gaia EDR3, and 2MASS data points are shown with red circles, green squares, orange triangles, cyan inverted triangles, and purple diamonds, respectively.

(An extended version of this figure is available.)

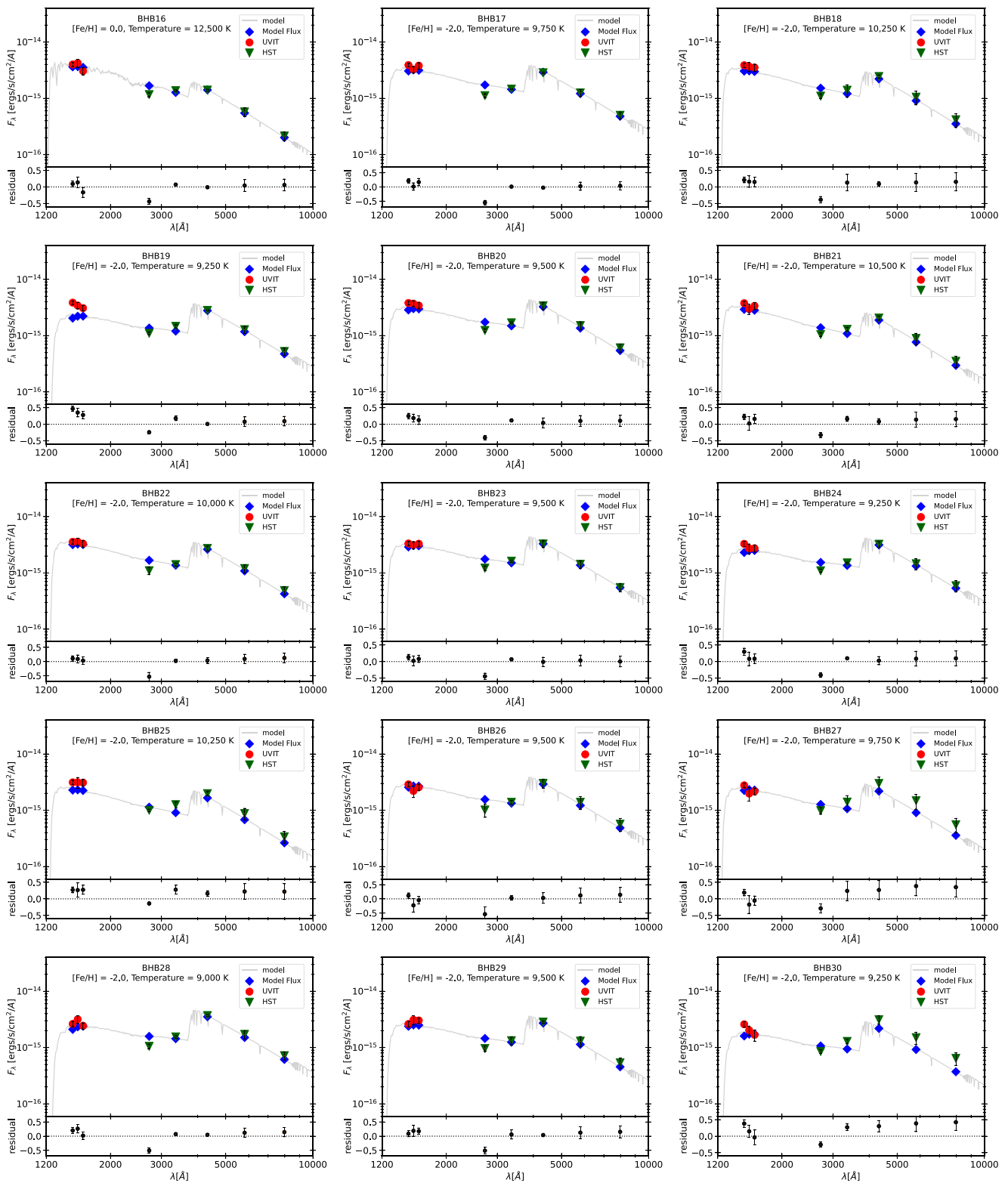


Figure 12. (Continued.)

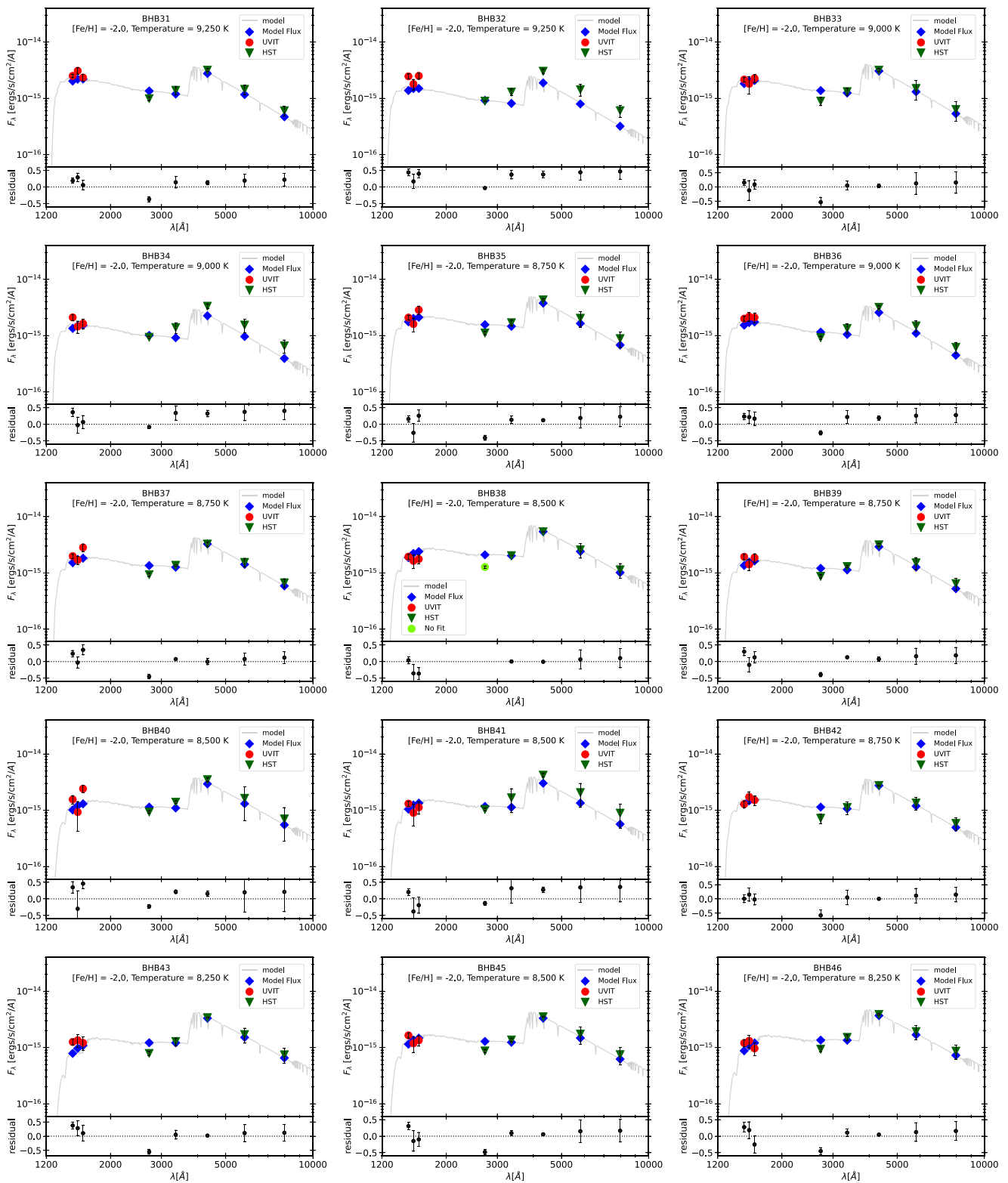


Figure 12. (Continued.)

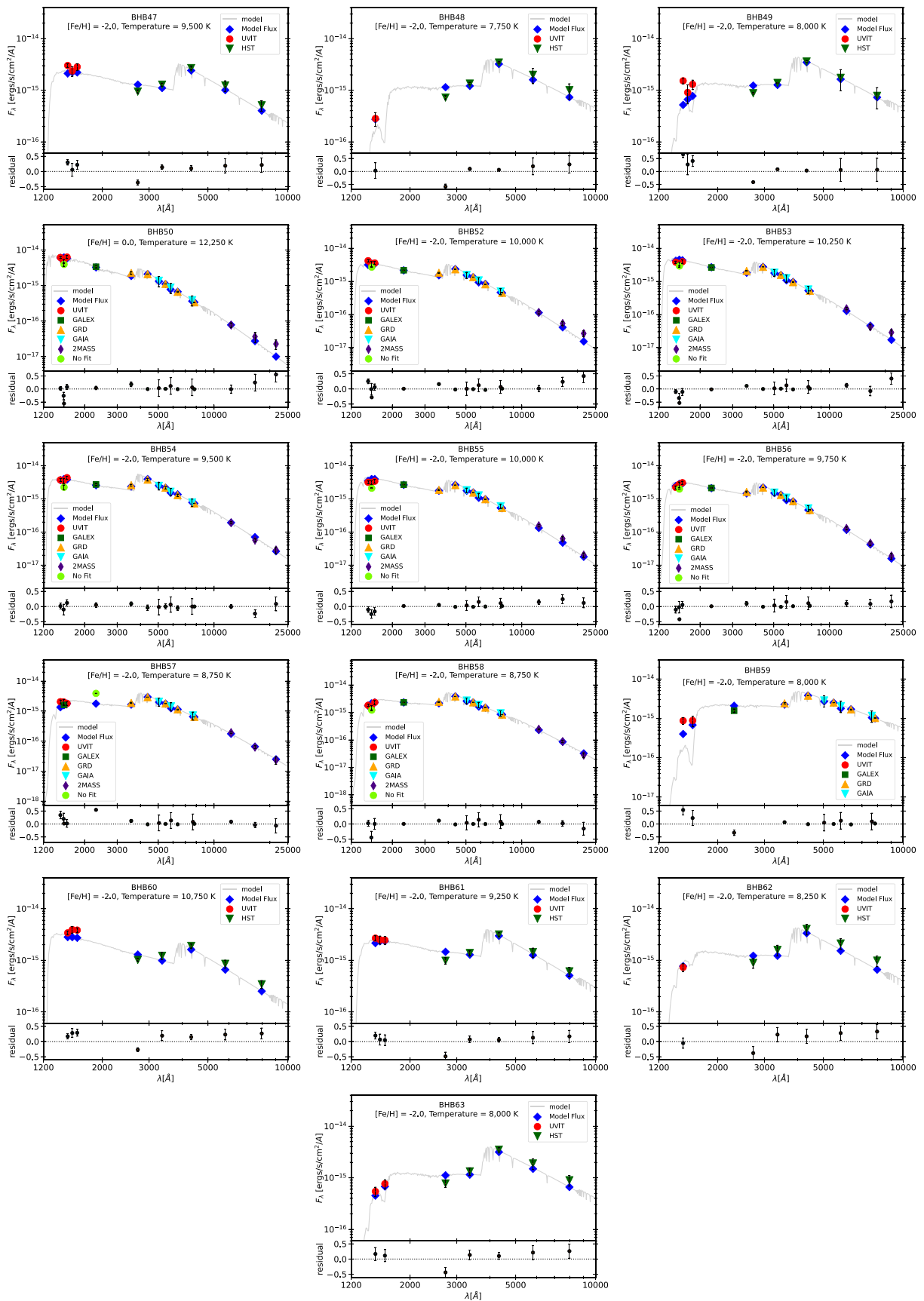


Figure 12. (Continued.)

ORCID iDs

Sharmila Rani  <https://orcid.org/0000-0003-4233-3180>
 Gajendra Pandey  <https://orcid.org/0000-0001-5812-1516>
 Chul Chung  <https://orcid.org/0000-0001-6812-4542>
 Snehalata Sahu  <https://orcid.org/0000-0002-0801-8745>
 N. Kameswara Rao  <https://orcid.org/0000-0002-8414-8541>

References

- Althaus, L. G., Miller Bertolami, M. M., & Córscico, A. H. 2013, *A&A*, **557**, A19
- Anderson, J., Piotto, G., King, I. R., Bedin, L. R., & Guhathakurta, P. 2009, *ApJL*, **697**, L58
- Astropy Collaboration, Price-Whelan, A. M., Sipőcz, B. M., et al. 2018, *AJ*, **156**, 123
- Astropy Collaboration, Robitaille, T. P., Tollerud, E. J., et al. 2013, *A&A*, **558**, A33
- Bayo, A., Rodrigo, C., Barrado Y Navascués, D., et al. 2008, *A&A*, **492**, 277
- Bekki, K. 2012, *ApJ*, **747**, 78
- Bonnarel, F., Fernique, P., Bienaymé, O., et al. 2000, *A&AS*, **143**, 33
- Brown, T. M., Bowers, C. W., Kimble, R. A., Sweigart, A. V., & Ferguson, H. C. 2000, *ApJ*, **532**, 308
- Brown, T. M., Cassisi, S., D'Antona, F., et al. 2016, *ApJ*, **822**, 44
- Brown, T. M., Ferguson, H. C., Davidsen, A. F., & Dorman, B. 1997, *ApJ*, **482**, 685
- Brown, T. M., Lanz, T., Sweigart, A. V., et al. 2012, *ApJ*, **748**, 85
- Brown, T. M., Smith, E., Ferguson, H. C., et al. 2008, *ApJ*, **682**, 319
- Brown, T. M., Sweigart, A. V., Lanz, T., et al. 2010, *ApJ*, **718**, 1332
- Brown, T. M., Sweigart, A. V., Lanz, T., Landsman, W. B., & Hubeny, I. 2001, *ApJ*, **562**, 368
- Busso, G., Cassisi, S., Piotto, G., et al. 2007, *A&A*, **474**, 105
- Carretta, E., Bragaglia, A., Gratton, R., D'Orazi, V., & Lucatello, S. 2009, *A&A*, **508**, 695
- Cassisi, S., Schlattl, H., Salaris, M., & Weiss, A. 2003, *ApJL*, **582**, L43
- Castellani, M., & Castellani, V. 1993, *ApJ*, **407**, 649
- Castelli, F., Gratton, R. G., & Kurucz, R. L. 1997, *A&A*, **318**, 841
- Castelli, F., & Kurucz, R. L. 2003, in *IAU Symp. 210, Modeling of Stellar Atmospheres*, ed. N. Piskunov, W. W. Weiss, & D. F. Gray (Cambridge: Cambridge Univ. Press), A20
- Chung, C., Yoon, S.-J., & Lee, Y.-W. 2011, *ApJL*, **740**, L45
- Chung, C., Yoon, S.-J., & Lee, Y.-W. 2017, *ApJ*, **842**, 91
- Clement, C. M., Muzzin, A., Dufton, Q., et al. 2001, *AJ*, **122**, 2587
- Dalessandro, E., Lanzoni, B., Ferraro, F. R., et al. 2008, *ApJ*, **677**, 1069
- Dalessandro, E., Salaris, M., Ferraro, F. R., et al. 2011, *MNRAS*, **410**, 694
- Dalessandro, E., Salaris, M., Ferraro, F. R., Mucciarelli, A., & Cassisi, S. 2013, *MNRAS*, **430**, 459
- D'Antona, F., Bellazzini, M., Caloi, V., et al. 2005, *ApJ*, **631**, 868
- D'Cruz, N. L., O'Connell, R. W., Rood, R. T., et al. 2000, *ApJ*, **530**, 352
- de Marchi, G., & Pulone, L. 2007, *A&A*, **467**, 107
- Dieball, A., Long, K. S., Knigge, C., Thomson, G. S., & Zurek, D. R. 2010, *ApJ*, **710**, 332
- Dondoglio, E., Milone, A. P., Lagioia, E. P., et al. 2021, *ApJ*, **906**, 76
- Dorman, B. 1992, *ApJS*, **81**, 221
- Dorman, B., O'Connell, R. W., & Rood, R. T. 1995, *ApJ*, **442**, 105
- Dorman, B., Rood, R. T., & O'Connell, R. W. 1993, *ApJ*, **419**, 596
- Ferraro, F. R., Paltrinieri, B., Fusi Pecci, F., Rood, R. T., & Dorman, B. 1998, *ApJ*, **500**, 311
- Fitzpatrick, E. L. 1999, *PASP*, **111**, 63
- Gaia Collaboration, Brown, A. G. A., Vallenari, A., et al. 2021, *A&A*, **649**, A1
- Gaia Collaboration, Helmi, A., van Leeuwen, F., et al. 2018, *A&A*, **616**, A12
- Gratton, R. G., Carretta, E., Bragaglia, A., Lucatello, S., & D'Orazi, V. 2010, *A&A*, **517**, A81
- Greggio, L., & Renzini, A. 1990, *ApJ*, **364**, 35
- Harris, W. E. 2010, arXiv:1012.3224
- Heber, U. 1986, *A&A*, **155**, 33
- Heber, U. 2016, *PASP*, **128**, 082001
- Heber, U., Edelmann, H., Lisker, T., & Napiwotzki, R. 2003, *A&A*, **411**, L477
- Hema, B. P., Pandey, G., Kurucz, R. L., & Allende Prieto, C. 2020, *ApJ*, **897**, 32
- Hidalgo, S. L., Pietrinferni, A., Cassisi, S., et al. 2018, *ApJ*, **856**, 125
- Hoyle, F., & Schwarzschild, M. 1955, *ApJ*, **121**, 776
- Hunter, J. D. 2007, *CSE*, **9**, 90
- Husfeld, D., Butler, K., Heber, U., & Drilling, J. S. 1989, *A&A*, **222**, 150
- Indebetouw, R., Mathis, J. S., Babler, B. L., et al. 2005, *ApJ*, **619**, 931
- Knigge, C., Zurek, D. R., Shara, M. M., & Long, K. S. 2002, *ApJ*, **579**, 752
- Koester, D. 2010, *MmSAI*, **81**, 921
- Lagioia, E. P., Milone, A. P., Marino, A. F., et al. 2021, *ApJ*, **910**, 6
- Lee, J.-W., Kang, Y.-W., Lee, J., & Lee, Y.-W. 2009, *Natur*, **462**, 480
- Lee, Y.-W., Joo, S.-J., Han, S.-I., et al. 2015, *HiA*, **16**, 247
- Lei, Z., Chen, X., Zhang, F., & Han, Z. 2015, *MNRAS*, **449**, 2741
- Lindgren, L., Hernández, J., Bombrun, A., et al. 2018, *A&A*, **616**, A2
- Marino, A. F., Milone, A. P., Przybilla, N., et al. 2014, *MNRAS*, **437**, 1609
- Marino, A. F., Villanova, S., Piotto, G., et al. 2008, *A&A*, **490**, 625
- McKinney, W. 2010, in *Proc. 9th Python Sci. Conf.*, ed. S. van der Walt & J. Millman (Austin, TX: SciPy), 51
- Mengel, J. G., Norris, J., & Gross, P. G. 1976, *ApJ*, **204**, 488
- Millman, K., & Aivazis, M. 2011, *CSE*, **13**, 9
- Milone, A. P., Bedin, L. R., Piotto, G., et al. 2008, *ApJ*, **673**, 241
- Milone, A. P., Marino, A. F., Dotter, A., et al. 2014, *ApJ*, **785**, 21
- Milone, A. P., Marino, A. F., Renzini, A., et al. 2018, *MNRAS*, **481**, 5098
- Milone, A. P., Piotto, G., Renzini, A., et al. 2017, *MNRAS*, **464**, 3636
- Moehler, S., Dreizler, S., Lanz, T., et al. 2011, *A&A*, **526**, A136
- Moehler, S., Landsman, W. B., Lanz, T., & Miller Bertolami, M. M. 2019, *A&A*, **627**, A34
- Moehler, S., Sweigart, A. V., Landsman, W. B., Hammer, N. J., & Dreizler, S. 2004, *A&A*, **415**, 313
- Monty, S., Puzia, T. H., Miller, B. W., et al. 2018, *ApJ*, **865**, 160
- Nardiello, D., Libralato, M., Piotto, G., et al. 2018, *MNRAS*, **481**, 3382
- Oliphant, T. E. 2007, *CSE*, **9**, 10
- Piotto, G., Bedin, L. R., Anderson, J., et al. 2007, *ApJL*, **661**, L53
- Piotto, G., Milone, A. P., Anderson, J., et al. 2012, *ApJ*, **760**, 39
- Piotto, G., Milone, A. P., Bedin, L. R., et al. 2015, *AJ*, **149**, 91
- Piotto, G., Villanova, S., Bedin, L. R., et al. 2005, *ApJ*, **621**, 777
- Postma, J. E., & Leahy, D. 2017, *PASP*, **129**, 115002
- Prabhu, D. S., Subramaniam, A., & Sahu, S. 2021, *ApJ*, **908**, 66
- Rani, S., Pandey, G., Subramaniam, A., Sahu, S., & Rao, N. K. 2020, *JApA*, **41**, 35
- Rani, S., Pandey, G., Subramaniam, A., Sahu, S., & Rao, N. K. 2021, *MNRAS*, **501**, 2140
- Raso, S., Ferraro, F. R., Dalessandro, E., et al. 2017, *ApJ*, **839**, 64
- Rauch, T., & Deetjen, J. L. 2003, in *ASP Conf. Ser. 288, Stellar Atmosphere Modeling*, ed. I. Hubeny, D. Mihalas, & K. Werner (San Francisco, CA: ASP), 103
- Rich, R. M., Sosin, C., Djorgovski, S. G., et al. 1997, *ApJL*, **484**, L25
- Riello, M., De Angeli, F., Evans, D. W., et al. 2021, *A&A*, **649**, A3
- Rosenberg, A., Recio-Blanco, A., & García-Marín, M. 2004, *ApJ*, **603**, 135
- Sahu, S., Subramaniam, A., Côté, P., Rao, N. K., & Stetson, P. B. 2019, *MNRAS*, **482**, 1080
- Schiavon, R. P., Dalessandro, E., Sohn, S. T., et al. 2012, *AJ*, **143**, 121
- Singh, G., Sahu, S., Subramaniam, A., & Yadav, R. K. S. 2020, *ApJ*, **905**, 44
- Sirianni, M., Jee, M. J., Benítez, N., et al. 2005, *PASP*, **117**, 1049
- Stetson, P. B. 1987, *PASP*, **99**, 191
- Stetson, P. B., Pancino, E., Zocchi, A., Sanna, N., & Monelli, M. 2019, *MNRAS*, **485**, 3042
- Subramaniam, A., Sahu, S., Postma, J. E., et al. 2017, *AJ*, **154**, 233
- Sweigart, A. V. 1997, *ApJL*, **474**, L23
- Tailo, M., Milone, A. P., Lagioia, E. P., et al. 2020, *MNRAS*, **498**, 5745
- Tandon, S. N., Hutchings, J. B., Ghosh, S. K., et al. 2017a, *JApA*, **38**, 28
- Tandon, S. N., Subramaniam, A., Girish, V., et al. 2017b, *AJ*, **154**, 128
- Taylor, M. 2011, TOPCAT: Tool for OPERations on Catalogues And Tables, ascl:1101.010
- Tremblay, P. E., & Bergeron, P. 2009, *ApJ*, **696**, 1755
- van der Walt, S., Colbert, S. C., & Varoquaux, G. 2011, *CSE*, **13**, 22
- Vasiliev, E. 2019, *MNRAS*, **484**, 2832
- Wenderoth, E., Alvarado, F., Liller, W., & Phillips, M. M. 1994, *PASP*, **106**, 718
- Werner, K., Deetjen, J. L., Dreizler, S., et al. 2003, in *ASP Conf. Ser. 288, Stellar Atmosphere Modeling*, ed. I. Hubeny, D. Mihalas, & K. Werner (San Francisco, CA: ASP), 31
- Whitford, A. E. 1958, *AJ*, **63**, 201
- Yong, D., & Grundahl, F. 2008, *ApJL*, **672**, L29